Deactivation of the Preferential Oxidation of CO in Packed Bed Reactor by 3D Modelling and Near-infrared Tomography

Faris Alzahrani, Hao Rusi*, Suttichai Assabumrungrat**, Daniel Luis Abreu Fernandes***, Farid Aiouache

Department of Engineering, Lancaster University, Lancaster LA1 4YW, U.K.

* School of Chemistry and Chemical Engineering, Queen University Belfast, Belfast BT7 1NN, Northern Ireland, U.K.

** Centre of Excellence in Catalysis and Catalytic Reaction Engineering, Department of Chemical Engineering, Faculty of Engineering, Chulalongkorn University, Bangkok 10330, Thailand

*** Department of Chemistry - Ångström Laboratory, Uppsala University, Uppsala 751 05, Sweden

Corresponding author:

Dr Farid Aiouache, Department of Engineering, Lancaster University, Lancaster, United Kingdom, LA1 4YW, E-mail: f.aiouache@lancaster.ac.uk

ABSTRACT

Scaling up the results on catalyst deactivation to industrial operations, where transport phenomena are of significance, is often not straightforward. The operations of industrial reactors are judiciously focused on the dynamics of the deactivation along the axial length of the reactors, which are generally known approximately. Processes of strong energy release or fast chemical kinetics, such as oxidation reactions, cracking, etc., are associated with a deactivation where the time characteristics of the flow and transports are of magnitudes of the deactivation time-on-stream. Local deactivation of the preferential oxidation of CO was investigated by three-dimensional modelling of flow, mass and heat transfers inside a packed-bed reactor and validated by near-infrared tomography. The profiles of deactivation were sensitive to the rates of deactivation, heat transfer by dispersion and intra-particle mass transfer. At pore scale of the packing, pronounced deactivation was revealed near the wall due to a preferential flow circulation. The deactivation progressed at the exteriors of the catalytic particles, particularly over the regions in contact with the convective flow. Unlike the mass dispersion, the heat dispersion promoted the deactivation by shifting the moving waves of deactivation upstream, leading to asymmetrical maps inside the catalytic particles.

Keywords:

Deactivation; preferential oxidation of CO; near-infrared imaging; spatially resolved; tomography; 3D modelling

1. Introduction

Catalyst deactivation is a common issue that leads to a decrease in productivity and deviations from normal operations of industrial processes. Process shutdown and catalyst replacement cost several billions of pounds per year worldwide, raising the need to develop more knowledge on the deactivation of catalysts at various scales of time and space. [1-3] Industrial packed-bed reactors (PBRs) are traditionally designed with physical access to averaged activity but with reduced access to local activity while reactions are taking place. The operations are consequently designed with oversized approximations to deal with uncertainties.

One approach that is gaining recognition to control the deactivation is by modelling the transport phenomena inside the PBR. This is true with ongoing developments of computational tools, which are allowing simulations of the three-dimensional (3D) geometries of hundreds of discrete packed pellets to be performed, imitating, to a reasonable extent, actual laboratory experiments. [4] These simulations, which are still insufficiently mature to simulate an industrial scale PBR, provide knowledge that would not be reached by the one-dimensional (1D) and two-dimensional (2D) models. It is important, however, to validate this knowledge by experimental insights into the PBR.

The simulation of catalyst deactivation in PBRs has been recurrently developed by coupling a model of the transport phenomena and functions of activity generated from experimental observations. Castillo-Araiza investigated the deactivation of mixed-oxide catalysts inside an industrial PBR for the partial oxidation of hydrocarbons. [5] The deactivation model of a sigmoidal profile along the axial length of the PBR confirmed the trends of the temperature and yield of the oxidation at transient operations. Wehinger et al. [6] developed a 3D model by coupling the rates of chemical kinetics and transports of momentum, mass and heat inside a PBR for the dry-reforming of methane over a rhodium-based catalyst. The 3D model generated a PBR of about one hundred spherical particles using the discrete element method (DEM) and allowed 3D visualization of regions with catalyst deactivation by carbon deposition. Likewise, Lopes et al. [7] developed a 3D and two-phase flow

model of a fluid catalytic cracking reactor. The trends of velocity, temperature and species produced non-uniform coke deposition over catalyst surfaces, underlining the importance of using the 3D modelling approach. This was particularly true at the entrance zone, where gradients of momentum and temperature were observed. Wang et al. [8] observed a uniform distribution of activity in a plate reactor for methanol steam-reforming. This reactor was reported to achieve higher performances than that of a PBR of a similar scale and this was explained by the reduced local spots of hot and cold zones. Quasi-isothermal operations were achieved when the catalyst was judiciously distributed in the PBR. Cheng et al. [9] reported an empirical model for prediction of the dynamic behaviours of species and deactivation by using experimental information on the temperature profiles along the axial length of a PBR. Similarly, Anastasov [10] described the deactivation in a PBR for the oxidation of o-xylene by observing the temperature trends along the axial length of the bed. The experimental data were fitted to a 2D model and allowed predictions of hot zones of high deactivation rates.

This series of works tested the uniformity of activity inside the reactors by placing multiple sensors at discrete locations of the PBR. This approach gives reliable trends of the activity profile but is time-consuming and likely to disturb the packing structure. Essentially, this approach gives a limited number of sampling zones which result in less certain gradients of temperature and species. A second approach relies on spatially resolved techniques. These techniques, being non-invasive, are looking promising in their application to gas–solid PBRs, where the signals retrieved from the gaseous phase are generally weak. Hofmann et al. [11] examined the deactivation in a wash-coated honeycomb monolith using a combination of transmission electron microscopy and X-ray absorption/diffraction spectroscopy at various spatial scales. The inhomogeneity of the catalytic coating was demonstrated to play a critical role in the development of local deactivation. The deactivation by coke deposits inside the straight channels of the H-ZSM-5 zeolite catalyst was confirmed by Devaraj et al. [12] using atom probe tomography, and by Chunga et al. [13] using a combination of *in situ* UV–vis and confocal fluorescence micro-spectroscopy techniques. Sanchez et al. [14] imaged the coke location at subnanometer scale of Pt−Re/γ-Al_2O_3 catalyst by using corrected scanning transmission electron

microscopy and enhanced energy dispersive X-ray spectroscopy. A technique based on 2D planar diffuse-reflectance near-infrared (NIR) imaging was developed by Aiouache et al. [15] to assess the activity of catalysts. A combination of high-throughput thermal imaging, spectroscopic imaging and principles of combinatorial chemistry allowed screening activity in a library of catalysts. Catalyst activity by thermal mapping was validated by mapping the surface hydroxyl overtones, as a tracing species, on cerium oxide catalyst during the steam-reforming of methane. The 2D technique was then extended to optical tomography for a semi-opaque packed bed adsorber of water vapour and PBR of hydrogen isotopic exchange process. [16-18]. NIR optical tomography has emerged in the recent years owing to developments in the laser technology for the telecommunication sector and imaging sensors of 2D array detectors, allowing the technique to be operated at spatiotemporal resolutions of sub-millimetres and sub-seconds. The principle of the technique consists of a plane that is illuminated, and the attenuated light is captured by 2D array detectors such as CCD cameras. Application of NIR imaging to gas-solid catalytic reactors emerged after sufficient maturity of comparative methods such as Raman imaging and IR imaging due to the penetration depth in scattering media that cannot be achieved in the mid-IR which encounters strong absorption. These applications of tomography offered simultaneous access to 3D spatial distributions of species and temperature, as illustrated in **Appendix A1**. Optical tomography was demonstrated to be a promising tool to access data on a region of interest, including mass dispersion, and validate existing models of flow in low AR packed beds. This achievement was made possible owing to recent developments in laser design, multispectral imaging and non-linear algebraic reconstructions. [18] Whereas current tomography needs only a single run, time resolution throughout the process is still essential, since catalyst deactivation varies widely depending on the time-on-stream of the deactivation system being monitored.

The present work aims to investigate dynamics of local profiles of activity in a PBR subject to rapid deactivations. A rapid deactivation, typically, drives time-on-stream characteristics that are of magnitudes of the transport time. To reach this aim, spatially resolved NIR tomography and 3D computational fluid dynamics (CFD) modelling, through a discrete packing, are employed. The

dynamic behaviour of local deactivation of preferential oxidation (PROX) of CO is investigated. The 2D planar NIR technique is extended to 3D diffuse tomography, where the distributions of water vapour (H_2O_V) flow are mapped, to access the results of interactions between catalyst activity and transport phenomena. The 2D planar technique provided valuable insights into the surface activity but did not entirely describe the process that occurred inside the PBR. By replacing the broadband light source with a fine bandwidth tuneable laser, NIR tomographic measurements of gaseous flow can be monitored by diffuse transmittance. A system for visualisation of the cross-sectional profiles of gaseous species, temperature and packing deactivation under dynamic conditions is developed. In the following sections, the kinetic model of the PROX of CO over Fe-Pt/γ-Al_2O_3 catalyst subject to deactivation is first investigated, as this information is missing for the dedicated catalyst. The mixed Fe-Pt catalyst over γ-Al_2O_3 was selected because it was reported to exhibit a reduced coverage of adsorbed CO intermediates, and by inference less deactivation than the single Pt/γ-Al_2O_3 catalyst, leading to a promising performance of the PROX at moderate temperatures (~ less than 473 K). [19-21] NIR tomography tests are then introduced for the PROX of CO and distribution maps of the species (herein H_2O_V) and temperature are retrieved and the underlying rates of fluid flow, mass and heat transports under catalyst deactivation are deduced. The 3D model is then developed and validated by results from the NIR tomography. A sensitivity analysis on the impacts of the flow, mass and heat transports on the local dynamics of deactivation is discussed.

2. Materials and methods

2.1. Near-infrared imaging tests

The design of experiments for the NIR tomography study was similar to the one cited in previous works, where the details on the experimental setup, procedure and validation of the results were discussed.[17-19] An integral PBR was filled with 3.5 g of 0.5% Fe-1% Pt/γ-Al_2O_3 catalyst. The catalyst was prepared by incipient wetness impregnation of γ-Al_2O_3 with a solution of platinic

chloride hexahydrate and iron nitrate. The PBR included two concentric tubes made of fused silica as shown in **Figure 1**. The inner tube was larger than that used previously (12 mm internal diameter and 39 mm length). The 5 mm thick annulus between the inner and outer tubes was designed to reach operations under adiabatic conditions by reducing the pressure of 10^{-6} mmHg with a diffusion pump. Pressure drop inside the PBR was measured by a differential pressure transducer (142PC02D, Sensortechnics GmbH). In addition, a humidity sensor (Exo Terra Digital Hygrometer, accuracy 2% at relative humidity >10%) was placed at the exit of the experimental setup. The gaseous phase temperature was measured by two thermocouples placed at the front and exit of the PBR.

The insights into the PBR by NIR tomography were run for a PBR of an AR of 13 and particle size of 0.850–1.000 mm. A typical run of deactivation was carried out at the inlet temperature of 413 K, feed flow rate of 670 cm^3 (NTP)·min^{-1} (i.e. weight-hourly space velocity of 11485 $cm^3 \cdot g_{cat}^{-1} \cdot h^{-1}$) and feed mixture composition of 1.1 mol% CO, 2.5 mol% O_2, 1.7 mol% H_2, and N_2 as carrier gas. Once a steady state was reached, the concentration of CO was step-increased to 1.4 mol% and the gases were analysed at the exit of the PBR by mass spectrometry at regular time-on-stream intervals.

Tomographic analysis was performed by collecting projected images from parallel beams that crossed the PBR at various angles. The NIR laser source (Santec TSL-510, modulating ranges from 1340 to 1440 nm) and the NIR detector camera (Mosir 950) were rotated by a servomotor around the PBR. The laser beam, which was first polarised, was collimated by a series of mirrors and cylindrical lenses to shape a rectangular sheet beam. A MATLAB-based code that relied on the adaptive algebraic reconstruction technique was developed to run the tomographic reconstructions of projected images (see **Appendix A1**). [18] The absorption coefficient of H_2O_V across the packing was calibrated by using a squared quartz cell, which was partially filled with Fe-Pt/γ-Al_2O_3 catalyst. The laser source was tuned to the spectral absorption line of H_2O_V at 1380.685 nm and the spectrum, which was free of scattering, located in the section above the packing, was validated by comparison with the Hitran database, [22] reaching an average deviation in the light transmittance of 0.4 mol% at 1% H_2O_V and

corresponding to average deviations of H_2O_V composition and temperature of 11.1% and 9.3% at a spatial resolution of sub-millimetres (i.e. 0.15 x 0.056 mm^2). [16]

2.2. Kinetic tests

The kinetic tests were carried out under differential flow (i.e. mass of catalyst 0.18 g, average pore size 3.5 nm, porosity 21% and surface area 218 $m^2\ g^{-1}$) to ensure low conversions of CO and quasi-isothermal operations. A small size of catalytic particles (i.e. 0.25 mm or AR of 48) was used to reduce the impact of mass and heat transfer limitations on the kinetic model. These limitations were later validated by using a smaller size of particles (i.e. 0.05 mm), as reported in section 3.1.1. The concentration of CO and temperature were varied from 0.5 to 1.1 mol% and from 413 to 473 K, respectively. Once steady-state conditions were reached, the concentration of CO was increased to 1.4 mol% at the stoichiometric concentration of H_2 in the feed. Before starting the experiments, the catalyst was reduced at 500 K for 2 hours under 1.0 mol% H_2 in N_2.

3. Results and discussions

3.1. Kinetics of the PROX of CO

The PROX of CO was selected as the model-reaction for the kinetic study of the deactivation dynamics. This reaction is typically carried out under dynamic operations (i.e. the fuel cells, automotive exhaust gases) [23-24] and is subject to catalyst deactivation due to the non-equilibrium of the surface coverage of CO, leading to critical effects on the performance and stability of the reactor. The oxidation reactions of CO (reaction 1) and H_2 (reaction 2) are associated with the reverse water-gas-shift (r-WGS) reaction (reaction 3), particularly at high temperature, reducing thus the conversion of CO. [25, 26]

$$CO+1/2\ O_2 \rightarrow CO_2 \qquad \Delta H_{r,298}{}^{o}{}_{C} = -283\ kJ/mol \qquad (1)$$

$H_2+1/2\ O_2 \rightarrow H_2O$ $\quad\quad$ $\Delta H_{r,298}{}^{o}C = -288$ kJ/mol (2)

$H_2 + CO_2 \leftrightarrow CO + H_2O$ $\quad\quad$ $\Delta H_{r,298}{}^{o}C = 41$ kJ/mol (3)

3.1.1. Mass and heat transfer limitations study

The potential gradients of concentration and temperature inside and outside the catalyst would lead to slow transfer rates of species and heat, affecting the results of the intrinsic kinetics. The limitation of transfer rates was investigated for two particle sizes of 250 μm (AR of 48) and 50 μm (AR of 240). The Weisz and Prater (W–P) criterion (Equation A.2.1) and Mears criterion (Equation A.2.2) were used to assess the relative effect of internal and external mass transfer limitations, respectively, as illustrated in **Appendix A2**. The existence of gradients of temperature inside the particles and in the film surrounding the particles, and relevant impacts on the model of kinetics, were assessed by the criteria of Damköhler numbers of the 4th order $Da_{i,(IV)}$ (Equation A.2.5) and 3rd order $Da_{i,(III)}$ (Equation A.2.6), respectively. These numbers measure the relevance of radial heat transfer limitations only when the axial one was assumed negligible for the size of particles used. [27]

Figure 2 (a) shows profiles of the W–P and Mears factors with temperature for the two particle sizes of 250 μm and 50 μm. The smaller size shows negligible resistance to mass transfer inside and outside the catalyst, while the larger size catalyst shows some internal resistance at temperatures higher than 480 K and external resistance at temperatures higher than 490 K, in agreement with the results of Kim et al. [27] and Ouyang et al. [28] **Figure 2 (b)** shows profiles of $Da_{i,(IV)}$ and $Da_{i,(III)}$ with temperature for the two sizes of particles. No resistance to heat transfer is observed in the profile of the smaller size, but some resistance to external heat transfer is visible at temperatures higher than 480 K, in agreement with the results of Ouyang et al. [28], validating the use of the particle size of 250 μm for the kinetics study.

3.1.2. Mechanism and kinetic profiles

The mechanism of the PROX of CO over noble catalysts such as platinum is known to include phenomena of multiple steady states (i.e. low and high reactive states) through an ignition and extinction hysteresis. [24] The low reactive state is dominated by the CO adsorption, particularly at low temperatures and high CO concentrations. During the low reactive state, O_2 exhibits a lower initial sticking coefficient than CO on platinum, and the surface of the catalyst is mainly covered by CO. The surface CO inhibits the adsorption of oxygen and hydrogen, inducing an ignition path. In contrast, the high reactive state is caused by a partial coverage of the dissociated oxygen and hydrogen, particularly at low CO concentrations and high temperatures. Hence, the extinction of PROX by CO is regarded as a deactivation that is a function of the surface coverage of CO and temperature. **Figure 3 (a)** shows steady-state profiles of the conversion of CO and selectivity to CO_2, as defined by Equation 4.

$$S_{CO_2} = \frac{r_{CO_2}}{r_{CO_2} + r_{H_2}} \tag{4}$$

Herein, r_{CO_2} and r_{H_2} are the rates of CO and H_2, respectively. **Figure 3 (a)** confirms the general observations of the kinetics of the PROX of CO with the temperature at a high reactive state and steady-state conditions. The oxidation of CO (Equation 1) was more competitive than the oxidation of H_2 (Equation 2) at low temperature only (less than the light-off temperature ~403 K). **Figures 3 (b_1 and b_2)** show transient profiles of the conversion of CO and selectivity towards the low reactive state, with time-on-stream and temperature, ranging from 403 to 473 K. The CO oxidation rate decreased rapidly with time-on-stream, while the selectivity kept approximately constant values. At low temperatures, H_2O_V formation was limited but not negligible, demonstrating coverage of the surface of the catalyst by CO and some hydrogen and oxygen. The CO_2 production was promoted after the light-off owing to the support from H_2, agreeing with the mechanism reported by Sirijaruphan et al.[18] and Amphlett et al. [29] (i.e. catalytic active sites covered preferentially by CO before light-off and H_2 after the light-off, promoting CO oxidation via hydroxyl intermediates). The stability in CO_2 selectivity suggests that the bimetallic Fe-Pt catalyst exhibited sufficient sites, making

the adsorption ability of H_2 and O_2 competitive with the adsorption of CO. The heat transfer limitation study in section 3.1.1 has shown the non-relevance of the heat transfer resistance in the BPR of the particle size of 50 μm (AR of 240) while some transfer limitation was observed at temperatures higher than 470 K for the particle size of 250 μm (AR of 48). The sensitivity of the PROX performance to temperature brings attention to the thermal management as discussed in section 3.4.

3.1.3. Kinetic model

The kinetic models that express changes in reaction rates along with the reactive states of the PROX include the power law, surface Eley–Rideal or surface Langmuir–Hinshelwood (LH) mechanisms, with conflicting results on the impacts of CO_2 and H_2O_V, as inhibiting or activating agents, on the rates of the PROX. [29-30] In the particular case of oxygen-rich feed, a zero-th order for oxygen and a positive order for CO were cited, with the latter order tending to increase to the first-order at high temperature. The power law model was cited for a selected range of operating temperatures and reactant concentrations and was therefore selected (Equations 5–7). [29] Some kinetic models expressed the hysteresis and associated extinguishing or igniting effects on the multiple states by adding a variable sticking probability function of a sigmoidal shape to the LH kinetic type. Herein, the deactivation behaviour is expressed by the model proposed by Jaree et al. [31] using a separate deactivation rate model (Equation 8). The separation of the deactivation behaviour from the main kinetic model allowed the investigation of a sensitivity analysis of the deactivation model to rates of mass and thermal transports in section 3.4. Since the inhibition of kinetics of reactions (1-3) was caused by CO adsorption only, the same activity term was assumed for each kinetics. Following the first-order in coverage mechanisms by Engel and Ertl, [32] Amphlett et al. [29] and Choi et al. [30] a power law kinetic model, which was associated with the three reactions and deactivation, is expressed by Equations 5–7.

$$r_1 = a\,k_1\,c_{CO}\,c_{O_2} \tag{5}$$

$$r_2 = a\,k_2\,c_{H_2}\,c_{O_2} \tag{6}$$

$$r_3 = a\,k_3\left(c_{CO}c_{H_2O} - \frac{c_{CO_2}c_{H_2}}{K_c}\right), \quad K_c = \exp\left(\frac{4577.8}{T} - 4.33\right) \tag{7}$$

The kinetics of catalyst deactivation was modelled by a power law expression relevant to self-deactivation by CO, assuming a negligible effect between the rate of reaction and reduction of the number of active sites for oxygen and hydrogen by the CO coverage.[33,34]

$$r_d = -\frac{da}{dt} = k_d c_{CO} = A_d \exp\left(-E_d/RT\right) c_{CO} \tag{8}$$

E_d and A_d are the activation energy and the pre-exponential Arrhenius factor of the deactivation rate, respectively. c is the concentration of species and K_c is the equilibrium constant of the r-WGS reaction.

A differential flow model was adopted to meet the requirements of reduced thermal resistance and pseudo-isothermal operations as expressed by Equation 9:

$$\frac{dc_i}{dt} = \sum_{j=1}^{3} r_{ji} \tag{9}$$

r_j is the stoichiometric rate of reaction j as expressed by Equations 5–8. The method of regression relied on changing the initial concentration of the feed and temperature while the composition of the species at the exit of the reactor was fitted to the model. Relevant sums of squares of residuals were minimised by the non-linear least squares method and the kinetic parameters were adjusted by the Marquardt approach. The trends of the model in terms of conversion and selectivity at a high reactive state in **Figure 3 (a)** and towards the low reactive state in **Figures 3 (b_1, b_2)** reasonably confirm its validity. The Arrhenius plots of rate constants, as illustrated in **Figure 4,** show higher activation energy of hydrogen oxidation than that of CO, demonstrating the impact of temperature on the relevance of H_2 oxidation in the PROX. The activation energy of H_2 oxidation and r-WGS are within the range of reported values, [25,29,30] whereas that obtained for CO oxidation – of 50216 J/mol – is lower than those reported for the case of a single CO oxidation, probably due to a weakening effect of Pt–alumina interactions with surface CO by hydroxylation via H_2 oxidation, leading to a facilitation

of the light-off at lower temperatures. [35] The rate constant of r-WGS is found to be comparatively small, reducing its contribution to the PROX of CO within the operating range. Accordingly, this result agrees with that obtained by Montreuil et al. [36] who found the activation energy of H_2 oxidation to be slightly higher than that of CO on Pt catalyst.

3.2. Mapping the PROX by NIR tomography

NIR tomography has been used to investigate the spatial profiles of temperature and species inside the PBR, with or without catalytic reactions. This helped to understand the phenomena of mass and heat transfers between the core and near-the-wall regions of PBRs of low AR. [16-18] Herein, the dynamic deactivation of the Fe-Pt/γ-Al_2O_3 catalyst during the PROX of CO was followed by screening the spatial maps of H_2O_V produced via hydrogen oxidation and potentially the r-WGS reaction. It was not possible to observe other species, as their optical absorption coefficients are of two to three magnitudes lower than those of H_2O_V in the NIR range.

The inlet temperature and CO composition were initially set to 413 K and 1.1 mol% respectively, in order to run the PROX at a sufficiently high reactive state. This state was held for 30 minutes at steady-state condition and the composition of CO was then step-increased to 1.4 mol%, allowing the self-inhibition of the PROX by CO to occur and progressively yielding the low reactive state. Self-inhibition by CO was associated with sufficient temperature gradients, allowing visual distinction to be made between the local hot and cold zones by NIR tomography.

The deactivation was expressed in terms of catalytic activity a, which states the acting condition of a catalyst at a given time-on-stream of the reaction. Activity was defined as the ratio of the reaction rate at a given time-on-stream to that of a non-deactivated catalyst. Herein, activity was approximated by the ratio of H_2O_V concentration at a given time-on-stream c_{H_2O} to that produced by a fresh (non-deactivated) catalyst $c_{H_2O,f}$, as expressed by Equation 10. The fresh catalyst corresponds to a non-deactivated catalyst at the high reactive state.

$$a = \frac{c_{H_2O}}{c_{H_2O,f}} \quad (10)$$

Figures 5 (a_1–a_3) show the profiles of the axial section maps of H_2O_V, from the bottom to the top of the PBR at 30 min, 60 min and 90 min, respectively. **Figures 5 (b_1–b_3)** and **(c_1–c_3)** illustrate relevant circumferentially averaged maps of H_2O_V concentration and temperature, respectively. More detailed cross-sections of the concentration of H_2O_V are found in the movie **mov$_1$**, added as supplementary material. The generation of H_2O_V was not homogeneous in the PBR, as shown in **Figures 5 (a_1)** and **(b_1)**. The flows of high and low concentrations of H_2O_V are differentiated by preferential channelling, as a result of the complex interplay between the rates of fluid flow, the transport phenomena of heat and mass, and chemical kinetics.[18]

Although some hot regions are visible at the centre of the PBR, the temperature distribution, which is represented by the circumferentially averaged maps in **Figure 5 (c_1)**, had a lesser correlation with the concentration of H_2O_V and presented a more uniform distribution. This was partially due to the exothermicity of the PROX process and inefficient transport of the generated heat by the flowing fluid of a low thermal inertia, particularly near the wall. The ignition took place at 13 mm from the inlet and was driven by oxidation of the unreacted CO and H_2, into CO_2 and H_2O_V respectively, downstream of the PBR. More explicitly, the increased oxidation rates generated sufficient heat to promote more CO desorption, increasing the rate of oxidation of H_2 into H_2O_V.

The NIR tomography allowed the discrimination of colder zones, particularly those close to the wall where a higher axial velocity, less mixing, and thus convective dispersion dominated. The hot zones were in the core packing area and started from catalyst particles that were not in contact with the wall, and progressively moved towards the wall of the PBR. The cooler areas would reflect a uniform velocity along both the axial and particularly the radial directions, whereas the warmer ones would reflect reduced flow and energy transfer. The weak distribution of energy was then the result of maldistribution and/or preferential channelling of the flow, in addition to heat and mass transports, and chemical kinetics under inhibition by catalyst deactivation.

Figures 5 (b_2, b_3) and **(c_2, c_3)** show circumferentially averaged maps of H_2O_V and temperature at time-on-stream of the PROX at 60 and 90 min respectively. Both the H_2O_V production and temperature decreased with time-on-stream in most of the regions. In some regions, particularly where the flow channelling took place, a larger decrease in H_2O_V was observed, driven by improved mixing. Local deactivation in terms of activity (i.e. Equation 10) provided additional information on regions where interactions of the rates of flow, mass and heat transfers took place. **Figure 6s (a–c)** show distribution maps of deactivation at 30, 60, and 90 min, respectively. More deactivation occurred towards the centre of the bed and was progressively expanding outwards with the time-on-stream. The deactivation was also prominent in regions of the bed where the flow channelling was pronounced. The spatial distribution of deactivation is seen reproduced in terms of H_2O_V maps. Profiles of the 1D circumferentially and radially averaged H_2O_V concentration and activity are shown in **Figures 7 (a) and (b)**, respectively. The profiles of activity in **Figure 7 (b)** were extended to 120 min of time-on-stream and show a travelling wave towards the downstream of the PBR. The maximum drops of activity with reference to inlet activity of the PBR were about 3, 9, and 22 % at 60, 90 and 120 minutes respectively. These drops were not discriminated in **Figure 6 (a)**, demonstrating the valuable information obtained by the spatial averaging, including propagation of deactivation in the PBR. This will help validation of the 3D model and understanding of the interplay between the rates of the flow and the transport of heat and mass under deactivation conditions. Overall, the results of the NIR imaging confirmed the existence of distinct rates of propagation of heat and mass along the PBR. The increase in CO at the front of the reaction zone resulted in interference of the two waves, temperature increase and catalyst deactivation.

3.3. Validation of spatially resolved deactivation profiles and sensitivity analysis by 3D modelling

A coupled model of the transport, kinetics of the PROX of CO and deactivation of the catalyst was used to assess local activity. The program code used expressions of a model under dynamics operations and included four differential equations, which included models of continuity, thermal and

mass balances, the kinetics and the deactivation. The model was validated and then extended to a parametric study of the effect of relevant parameters on local activity along the PBR, including: (1) the activation energy of the catalyst deactivation rate, (2) the concentration of catalyst in the PBR and (3) the feed flow rate, and by inference the dispersion rate; and (4) the intra-particle mass transfer rate.

Previous works that applied 3D modelling and deactivation used a slow deactivation model of sufficiently large time-on-stream compared to the residence time in the PBR. [6,37] Jaree et al. [38] reported that deviations could exist between the predictions of heterogeneous models and homogeneous models for PBRs, particularly at low flow regimes of limited heat and mass transfer rates. Herein, the deactivation in the PBR is investigated by a 3D heterogeneous model under a reaction time that is comparable with the deactivation time.

3.3.1. Packing generation by DEM

The 3D heterogenous model relied on building a cylindrical PBR containing discrete spherical particles. The particles were assembled by 3D DEM and the conditions were set to match those used for the NIR tomography. A PBR of 10 mm internal diameter, which included two sections of 17.5 mm and 5 mm lengths, was built by packing 2031 spherical particles of 1 mm size (i.e. AR of 10). The shorter section of the PBR was added to ensure the development of flow free of an entrance effect. The particle flow code PFC^{3D} (Itasca, Ltd.) was used to write a DEM code in the embedded FISH programming language and generate a randomly structured packing. Several variables of both the wall and the particles (i.e. stiffness, density and friction coefficients) were processed to reach a suitable compaction of the particles, as illustrated in **Table 2**. The DEM code was set to calculate the positions, momentum, spins and trajectories of the particles and their interactions, whilst the PBR was populated with the particles, to reach a truly random structure. The code followed an iterative method to calculate the position of each particle until reaching a limit of stability of settlement (i.e. the overall force on each particle was set to be less than 10^{-7} N). The

output of the DEM simulation was a matrix of data in Cartesian coordinates that located the position of the centre of each generated particle. The matrix was rendered in CAD format and exported to the CFD package.

3.3.2. Porosity validation

The structure of the PBR was validated by comparing its porosity with literature models.[39, 40] The volume of the packing (i.e. 3D matrix) was discretised into elements of volume by using the domain index implemented in the CFD package. The discretisation by 3D unstructured meshing, as shown in **Figure 8**, used tetrahedral cells of a maximum spatial resolution of 25 elements per particle diameter. The contact points between the particles released skewed elements which were reduced by shrinking the size of particles by about 0.5%. [41] Setting a higher shrinkage, while computationally time-consuming, did not produce more refined results because the small clearance between the particles was associated with a considerable pressure loss. The elements of volume, which were defined by the length of the edge, the thickness of the boundary layer at particle-to-fluid or wall-to-fluid, the size and rate of expansion of the elements, were constantly refined at particle-to-particle and particle-to-wall contact points until reaching results of pressure drops free of mesh size (see sections 3.3.3 and 3.3.4). These elements were then allocated values of zero and one for the inter-particle space and occupied space, respectively. A space resolution of 0.04 x 0.04 x 0.04 mm^3 was found satisfactory to observe the variation of local porosity ϕ_{3D} at reduced distortions, particularly in the regions of low meshing resolution. Thus, the 3D volumetric data were reduced into a 2D surface porosity map ϕ_{2D}, 1D line porosity ϕ_{1D} and overall porosity ϕ_{ave} by averaging along the angular coordinate (Equation 11), radial coordinate (Equation 12) and axial coordinate (Equation 13), respectively, allowing the prediction of flow patterns at multiple dimensions in space and access to data which would not be observed through the 3D structure.

$$\phi_{2D}(r,h)=\frac{\int_0^{2\pi}\phi_{3D}(r,h,\theta)\theta\, d\theta}{\int_0^{2\pi}\theta d\theta} \tag{11}$$

$$\phi_{1D}(r)=\frac{\int_0^{L}\int_0^{2\pi}\phi_{3D}(r,h,\theta)\theta h\, d\theta dh}{\int_0^{L}\int_0^{2\pi}\theta h\, d\theta dh} \tag{12}$$

$$\phi_{ave}=\frac{\int_0^{R}\int_0^{L}\int_0^{2\pi}\phi_{3D}(r,h,\theta)\theta hr\, d\theta dhdr}{\int_0^{R}\int_0^{L}\int_0^{2\pi}\theta h\, r\, d\theta dhdr} \tag{13}$$

where r, h and θ are the cylindrical coordinates of porosity. The results of the 2D surface map, 1D radial distribution and overall porosity values are shown in **Figures 9 (a) and (b),** respectively. The profile of the porosity map in **Figure 9 (a)** shows periodic distributions along the radial direction, with larger values near the wall and progressively damped towards the central axis. While limited data on local porosity were available in the regions close to the central axis for 2D averaging, these changes revealed a non-homogeneous distribution with some loose structure near the central axis as shown in **Figure 9 (b**). The 1D line of **Figure 9 (b)** follows the general trends of porosity for low AR PBRs (i.e. clear damping towards the central axis) and shows average deviations of ~6.1 and 1.1 % from the models by Giese et al. [39] and Zou et al. [40], respectively. This deviation was attributed to the remediation of skewed contact points of particles and uncertainty in offsetting the porosity at the top layer of the randomly settled particles in the PBR.

3.3.3. Model description

The 1D pseudo-homogeneous model by Jensen and Ray [41] for oxidation of CO was extended to a 3D heterogeneous model for the PROX, which included momentum, heat and mass balances in the PBR. The model was then validated by comparison with the data from NIR tomography. The flow was assumed to be laminar and the PBR was operated under adiabatic conditions. The temperature-dependent physical properties (i.e. density, viscosity, diffusivity, thermal conductivity and thermal capacity) relevant to both the gaseous and the catalytic phases were approximated by empirical functions as reported in **Table 1**. The Navier–Stokes equation for momentum balance, and the

continuity equation for the mass conservation, including both the pressure and viscous forces, are expressed by Equations 14 and 15, respectively.

$$\rho_g\left(u\cdot\nabla u\right)=-\nabla pI+\nabla\cdot\left(\mu\left(\nabla u+\left(\nabla u\right)^T\right)-\frac{2}{3}\mu\left(\nabla\cdot u\right)I\right) \quad (14)$$

$$\rho_g\nabla\cdot u=0 \quad (15)$$

where ρ_g is the density of the gaseous phase, p is the static pressure, μ is the dynamic viscosity, u is the velocity vector and I denotes the identity matrix. Atmospheric pressure at the exit, fixed velocity at the inlet, and no-slip conditions at the solid–gas contact points were assumed. The modules of the transport of diluted species and heat transfer in fluids of the COMSOL user-interface were set under transient operations. The mass balance model for the gaseous phase included mass transfer by both diffusion and convection (Equation 16), whereas the mass transfer model for the catalytic phase combined the diffusion and the catalytic reaction in the catalytic particles (Equation 17).

$$\frac{\partial c_{i,g}}{\partial t}+\nabla\cdot\left(-D_{i,g}\nabla c_{i,g}\right)+u\cdot\nabla c_{i,g}=0 \quad (16)$$

$$\frac{\partial c_{i,s}}{\partial t}+\nabla\cdot\left(-D_{i,s}\nabla c_{i,s}\right)=\sum_{j=1}^{3}r_{ji} \quad (17)$$

The model of diffusivity in the solid phase $D_{i,s}$ included the textural parameters according to models of non-structured porous networks and was estimated according to Equations 18 (a-c), by considering both Knudsen D_i^K and bulk solid types of diffusion D_i^b.

$$\frac{1}{D_{i,s}}=\frac{1}{D_i^b}+\frac{1}{D_i^K} \quad (18a)$$

$$D_i^b=\frac{\varepsilon_s D_{i,g}}{\tau_s} \quad (18b)$$

$$D_i^K = \frac{2}{3} r_p \sqrt{\frac{8RT}{\pi M_i}} \frac{\varepsilon_s}{\tau_s} \quad (18c)$$

The diffusivity values of H_2O, H_2, CO, CO_2 and O_2 species in the gaseous phase $D_{i,g}$ were approximated to the molecular diffusivity of these species due to the low concentrations used, M_i is the molecular weight, r_p is the average pore radius and ε_s and τ_s are the textural parameters of catalytic particles in terms of porosity and tortuosity respectively.

The analogous heat balance model included thermal transfers by both conduction and convection in the gaseous phase (Equation 19) and by conduction in the catalytic phase (Equation 20). This was later coupled to the heat source by the chemical reactions.

$$\rho_g C_{pg} \frac{\partial T}{\partial t} + \nabla \cdot \left(-k_g \nabla T\right) + \rho_g C_{pg} u \cdot \nabla T = 0 \quad (19)$$

$$\rho_s C_{ps} \frac{\partial T}{\partial t} + \nabla \cdot \left(-k_s \nabla T\right) + \sum_{j=1}^{3} \Delta H_{r,j} r_{ji} = 0 \quad (20)$$

where C_{pg} and C_{ps} are the heat capacity of the gaseous and solid phases, respectively, k_g and k_s are the thermal conductivity of the gaseous and solid phases, respectively, r_{ji} and $\Delta H_{r,ji}$ are the stoichiometric rate and the heat generated by reaction j, respectively, as expressed by Equations 5–7. The values of the physical properties are assembled in **Table 1**.

The discretisation into finite elements allowed integration of the governing equations via sets of difference equations by using the generalized minimal residual method with the Geometric Multigrid preconditioner algorithm. This algorithm approximated the solution by using the vector in a Krylov subspace at reduced residual (i.e. satisfactory convergence with relative tolerance of 0.01%). The built-in meshing module of Comsol was used and the Adaptative Mesh Refinement procedure allowed shapes of the elements to be dominated by tetrahedral domains and triangular surfaces. The impact of size of the elements on the viscous forces, particularly at the contact points of particles, was validated by carrying out by a mesh convergence test, monitoring the pressure values at three

arbitrary locations and using the Grid Convergence Index (GCI) as described in **Appendix A3.** A solution, irrespective of mesh size, was reached when the GCI was below 4.2%. [44] The mesh refinement was extended to concentration of species until a relative deviation of less than 4.3% was reached. The computation was carried out first for modelling fluid flow at steady-state operations (Equations 14 and 15) and the results were used as initial values for computation of the heat and mass transfer model at transient operations. Initially, the PROX was set at a high reactive steady state and then the deactivation process was switched on when the CO concentration was step-increased, causing transient profiles of temperature, concentration and catalyst activity. In the following, an analysis of both local activity and temperature was carried out after the increase in CO concentration. It is followed by a parametric study on the effects of the activation energy of the deactivation rate constant, the concentration of catalyst, diffusivity of the reactive species inside the gaseous phase and catalyst on the local deactivation. The simulation was carried out using COMSOL Multiphysics 5.2.a and a 512 GB RAM computer server.

3.3.4. Flow profiles and validation

The flow profile in the PBR was assessed by comparing the pressure drops ΔP in the PBR (Equation 21) predicted by the model with those from literature models, which are known to be suitable for low AR PBRs, including the Ergun, Zhavoronkov and Reichelt models. [45]

$$\Delta P = \frac{\Delta p}{L}\frac{d}{\rho_g {u_s}^2} \quad (21)$$

where d is the particle diameter, u_s is the superficial velocity and L is the length of the bed. The profile of pressure drops with the flow in terms of the Reynolds number in **Figure 10 (a)** shows agreement with the Reichelt model, particularly at a high flow regime. The axial section map of velocity at conditions similar to the experimental tests of deactivation in **Figure 10 (b**) shows an increase in local velocity of up to 10 times the inlet velocity in some particular zones between the particles, but does not enable the observation of the overall distribution of the velocity over the PBR. The

circumferentially averaged velocity, however, as shown in **Figure 10 (c),** shows periodic variations along the PBR, creating a flow of a tortuous nature between the particles, and confirms the profiles of porosity in section 3.3.2. The velocity trends released some by-pass circulation of the flow near the wall due to high porosity in this zone. The zones of efficient mixing were observed through the radial flow in **Figure 10 (d_1)**, where there is pronounced flow in regions close to the wall of the PBR, particularly around the particles as shown **in Figure 10 (d_2)**. Other zones at contact points of the particles exhibited small flows, revealing flow with a stagnancy behaviour.

3.3.5. Effect of increase in CO concentration on local deactivation

Similar to the profiles of the conversion of CO and temperature obtained by NIR tomography (Figures 5–7), those computed by the modelling show reaction zones between the light-off temperature and the maximum temperature. At the front of the reaction zone, the temperature increased to the adiabatic value, whereas downstream zones exhibited high temperature waves up to 30 min before decreasing due to the deactivation and cooling by flow dispersion. **Figures 11 (a_1-c_1)** illustrate profiles of the axial cross-line at 1 mm from the centre of the PBR of temperature, activity and conversion of CO, respectively, at various times-on-stream. The relevant axial cross-section maps at a single time-on-stream (i.e. 120 min) are shown in **Figures 11 (a_2-c_2)**. **Figure 11 (a_1)** shows that the front of the reaction zone, at approximately 10 % of the full temperature rise, took place about 6 mm from the inlet of the reactor and then progressively moved towards the downstream of the reactor.

The deactivation is reflected by inhibition of the PROX. Distinct thermal and local activity profiles at various locations of the PBR were released. The sectional map of temperature in **Figure 11 (a_2)** shows hot spot zones of insufficient mixing (non-uniform axial and/or radial velocities), such as those in the centre of the PBR. As the reaction progressed towards deactivation, the bed cooled down, particularly at the centre of the packing (not shown). The cross-lines of local activity in **Figure 11 (b_1)** followed similar trends to the temperature as relevant waves propagated towards the exit of the PBR. Intra-particle deactivation was homogeneous at the front of the reaction zone but was notably

heterogeneous in the core of the reaction zone. The unreacted CO, as illustrated in **Figure 11 (c_1)**, shows trends of decrease that reproduce those of the temperature, but the values of the gradient of CO concentration in the reaction zone were higher than those observed by NIR tomography. CO reacted more with surface oxygen as it entered the catalytic zone, potentially very present in this zone, to release temperature waves having a positive effect on the rates of H_2 oxidation.

The 3D views and cross-sectional maps of activity in **Figures 12 (a_1 and a_2)**, respectively, and temperature in **Figures 12 (b_1 and b_2)**, respectively, are shown along with detailed descriptions of activity in the supplementary materials **(**i.e. **mov2 and mov3).** The cross-sectional maps of activity in **Figures 12 (a_1, a_2)**, positioned 15 mm from the inlet, show the activity being affected in the thin zones surrounding the particles. In these zones, distinct regions of lower conversions of CO than those in the interior of the particles are visualised (see **Figure 11 (c)**). More deactivation occurred in regions near the wall of the PBR, where high velocity and porosity took place as discussed in sections 3.3.2 and 3.3.4. The higher velocity near the wall promoted local thermal dispersion by advection – as illustrated by the lower temperature trends near the wall in **Figures 12 (b_1, b_2)** – and, by inference, local deactivation. Additionally, the dynamics of deactivation are observed at inter-particle (packing pores) and intra-particle pores, and both produced asymmetrical trends of activity. These trends were probably due to distinct dispersion rates by advection surrounding the particles (i.e. higher interstitial velocity values and thus dispersion rates at the front sides of the particles). This is an interesting finding, since the heterogeneous rates could be subject to thermal expansion and contraction and further catalyst attritions or temperature runaways (i.e. beyond the objectives of this work). Overall, both the 1D axial profiles and cross-sectional 2D profiles of activity obtained by 3D modelling reasonably reproduced the trends obtained by NIR tomography in **Figures 5 and 6**.

These results of mass dispersion validated the finding of section 3.3.4 on inefficient mixing in the centre of the bed and circulatory flow near the wall. The 3D model offered spatially resolved data of temperature and species distributions inside the PBR and efficiently discriminated between zones of

distinct mixing, allowing the use of the model to predict the behaviours of the PBRs subject to deactivation.

3.4. Sensitivity analysis

The interactions of the heat and mass transports with the PROX under deactivation were investigated in terms of the relative relevance of rates of deactivation, the kinetics of the PROX, and mass and heat transports.

3.4.1. Influence of the activation energy of deactivation rate constant on local deactivation

The relevance of the deactivation rate during the PROX under deactivation was investigated by changing the activation energy of the deactivation rate constant E_d under conditions that were similar to those in section 3.3.4. **Figures 13 (a_1, a_2)** show cross-line profiles of activity and temperature along the axial length of the PBR. The activity decreased at the front inlet of the PBR when the activation energy was decreased. As the front of the PBR was progressively less active, the decrease in activity propagated to the reaction zone through a moving wave. The lower values of activation energy accelerated the rate of deactivation and inhibited the PROX reaction, and thus less energy was released, which in turn inhibited the deactivation, as shown by the rise of activity downstream of the PBR. Greater deactivation occurred in the regions of high temperature rise, as shown in **Figure 13 (a_2)**. At the end of the PBR, profiles of increased activity are observed as the temperature reached the adiabatic rise.

3.4.2. Influence of mass of catalyst on local deactivation

The relevance of the chemical kinetics of the PROX under deactivation was investigated by changing the mass of the catalyst and constant flow residence time. The mass of catalyst was varied by random dilution of the catalytic packing using non-catalytic γ-Al_2O_3 particles of similar properties to the catalytic γ-Al_2O_3. **Figure 13 (b_1)** shows the axial profiles of deactivation along the PBR for three

catalyst concentrations and conditions similar to those in section 3.3.4. At low concentration, the reaction zone covered a large area of the PBR and was associated with a reduced deactivation. At high values of catalyst concentration, the activity decreased in regions of high temperature rise and then increased downstream as the temperature reached the adiabatic rise, as shown in **in Figure 13 (b_2)**.

3.4.3. Influence of mass and thermal diffusivities of the carrier gas on local deactivation

The relevance of the local flow of dispersion during the PROX under deactivation was investigated by changing the mass and thermal diffusivities of the reactive mixture. The diffusivities were approximated to those of the carrier gas due to high dilutions of the reactive mixture. The simulation was first set to conditions that were similar to those in section 3.3.4 and then the nitrogen gas carrier was replaced by helium gas. The mass and the thermal diffusivities increased by about three and five times, respectively, as illustrated in **Table 1**, when the PROX was run using helium gas. The deactivation took place close to the inlet in the case of helium, as shown in **Figure 13 (c)**, by stretching the reaction zone and thus moving the deactivation wave towards the inlet.

3.4.4. Influence of intra-particle mass transfer on local deactivation

The high thermal conductivity of the γ-Al_2O_3 support did not allow noticeable gradients of temperature within a single particle when heat transfer limitations were investigated in section 3.1.1, leaving the heat transfer to be predominantly controlled by the external flow conditions in the PBR, particularly at temperatures higher than 480 K. This was not the case of the intra-particle concentration gradients, which were non-negligible at conditions of the PROX process, affecting both the chemical kinetics and the deactivation.

The effect of the intra-particle mass transfer on local deactivation profiles was investigated at conditions similar to those that were set in section 3.3.4, except that the diffusion coefficient in the pores was set to one-tenth and one-hundredth of the typical value (i.e. characteristic diffusion time ($d_p^2/D_{i,s}$), ranging from 0.3 to 33.3 seconds), corresponding to the conditions of alumina supports of

microporous structure. **Figure 13 (d)** shows axial cross-line profiles of activity along the PBR for the additional two values of catalyst diffusivities. The intra-particle mass transfer affected the activity profiles in a similar way to that in which it affected the concentration profiles. It affected the activity inside the catalyst particles and the surrounding zones of distinct thin layers of deactivation, as shown in **Figure 12 (a_2)**. The deactivation was pronounced in the thin exterior layer over the sides of particles that were frontally exposed to the gas flow. The deactivation was also pronounced when differences in diffusivities in the solid and the gas phases were significant, as shown in **Figure 13 (d)**. Such trends took place because the rich presence of CO in the feed first deactivated in zones close to the exterior of the particles, and progressively moved inwards with the time-on-stream, as shown in **Figure 11 (b)**. The high values of diffusivity, which were desired at high temperature PROX reactions to reduce the presence of H_2O_V and CO_2 products inside the particles, shifted the local deactivation towards the inlet, as shown in **Figure 13 (d)**. Low values of diffusivities developed pore resistance to CO, leading to an interesting challenge to balance between the reaction rate, deactivation rates and mass transports.

3.4.5. Influence of the aspect ratio on local deactivation

Since the structural porosity and local flow are sensitive to the confining wall in low AR PBRs, the deactivation was examined in a PBR of AR of 5 (i.e. particle diameter of 2 mm) at conditions that were similar to those in section 3.3.4, including the intra-particle diffusion time. **Figure 13 (e)** shows the axial cross-line profiles of activity along the PBR for values of AR of 5 and 10. The profiles of activity of the PBR of 5 released pronounced trends of deactivation which broadened towards the inlet, demonstrating the relevance of the thermal dispersion (as discussed in section 3.4.3) on the extension of the reaction zone in the PBR. Previous work [45] has shown that a PBR with an odd number of AR would exhibit less circulation of the flow near the wall and more distribution in the zones close to particle-to-particle contacts than a PBR with an even number of AR. Unlike the PBR of 10, the PBR of AR 5 showed more circulation at the centre of the PBR and less circulation near

the wall, which confirms previous results and explains the relevance of dispersion to shape the trends of deactivation.

3.5. Discussion

Studies at laboratory scale on catalyst deactivation are of less relevance when extended to industrial scale operations, where transport phenomena are of significance. In addition, the operations of industrial reactors are reasonably focused on the dynamics of the deactivation along the axial length of the PBR, which are often only known approximately. Spatial trends of dynamic deactivation are therefore often cited in works carried out at laboratory scale, but are barely cited in the open literature. Typically, the deactivation takes place for a greater time-on-stream than the response from the mass and thermal transports. Some reactions, however, particularly those with a strong energy release (oxidation reactions, cracking, pyrolysis, etc.), are associated with a deactivation where the time characteristics of the flow and transports are of magnitudes of the deactivation time.

A comparison between the results obtained experimentally using NIR tomography and those obtained by the model at conditions similar to those in section 3.3.4 is illustrated in **Figure 14**. Both experimental and model profiles of the axial activity exhibit the front of the reaction zones that took place at about 4 mm and 6 mm from the inlet of the PBR, respectively, and then progressively moved towards the exit of the PBR. These profiles are reasonably similar but the model profile predicted a deactivation about 12.5% higher than that obtained by NIR tomography. The trends show zones of less activity at the front inlet of the PBR and these zones then propagated to the reaction zone. Activity then increased downstream as the relevant temperature reached the temperature rise. Among the parameters of the sensitivity analysis to which the deactivation was significantly sensitive was the activation energy of the deactivation rate constant, probably due to the exponential profile of the relation between the activation energy of deactivation and activity. The value of the activation energy of deactivation was therefore varied to fit the values of activity by NIR tomography. **Figure 14** shows

a deviation of 3.1% between the experimental data and the model when the activation energy of deactivation was reduced by 10%. The sources of this deviation could be caused, in addition to the aforementioned approximations and assumptions made for the 3D model, by the development of limitations of the external mass and heat transports, particularly at temperatures higher than 470 K. Overall, the activity decreased not only at the front inlet of the PBR but also at the bulk of the reaction zone when the activation energy of deactivation was decreased. This was driven by an acceleration of the rate of deactivation, inhibition of the PROX reaction, and reduction in the released energy, which in turn inhibited the deactivation.

4. Conclusions

The local deactivation inside a gas–solid PBR was investigated by 3D modelling and validated by experimental NIR imaging. The kinetic data for the Fe-Pt/γ-Al_2O_3 catalyst were obtained at dynamic conditions. The conversion of CO oxidation was strongly dependent on the reaction temperature and CO composition in the feed. The trends of temperature, including the light-off temperature and maximum temperature, obtained by 3D modelling were in reasonable agreement with the experimental data by NIR tomography. Non-uniform deactivation was investigated by a sensitivity analysis of the deactivation to several parameters, including the activation energy of the deactivation rate, mass and heat dispersion rates, intra-particle mass transfer rate and AR of the PBR. A decrease in either the activation energy of the deactivation rate or the concentration of catalyst increased the deactivation rate, inhibited the PROX rate and reduced the release of energy, which in turn inhibited the deactivation downstream. At pore scale of the packing, a greater deactivation occurred near the wall due to higher circulation of flow and dispersion for the PBR of AR of 10. Deactivation was also pronounced in thin layers at the exterior of the catalytic particles in contact with the flow. Unlike the mass dispersion rate, the heat dispersion rate promoted deactivation by shifting the wave upstream of the PBR, leading to asymmetrical deactivation maps inside the catalytic particles.

Local deactivation and the underlying phenomena of mixing, mass waves and thermal waves were experimentally observed and quantified. The spatial resolution of NIR imaging was of importance to validate the results of the 3D model. Ongoing work is intended to extend the NIR tomography to mid-infrared imaging, where species other than H_2O_V, such as CO, CO_2, and NO_X, exhibit sufficient extinction coefficients to be used as tracing species.

Acknowledgments

The authors would like to acknowledge the support for funding provided by the Department of Education and Learning (DEL) and Saudi Arabia Government and Lancaster University starting grant. S. Assabumrungrat also would like to acknowledge the "Research Chair Grant" National Science and Technology Development Agency (NSTDA).

Symbols and abbreviations

a: Activity [-]

a_s: Surface area of catalyst particle [m^2 kg^{-1}]

Abs : Absorbance [-]

A_d: Arrhenius constant of deactivation rate constant [m^3 $mol^{-1}s^{-1}$]

c_i: Concentration at a given time-on-stream [mol m^{-3}]

$c_{i,f}$: Concentration produced by a fresh catalyst (activity of unity value) [mol m^{-3}]

C_p: Heat capacity [J kg^{-1} K^{-1}]

c_0 : Speed of light [m s^{-1}]

D_i: Diffusivity [m^2 s^{-1}]

D_i^K : Knudsen type diffusion coefficient [$m^2\ s^{-1}$]

D_i^b: Bulk solid type diffusion coefficient [$m^2\ s^{-1}$]

Da_i: Damköhler number [-]

d : Diameter of catalyst particle

E: Activation energy [$J\ mol^{-1}$]

E_d: Activation energy of deactivation rate constant [$J\ mol^{-1}$]

E_i: Lower state energy [cm^{-1}]

e_a^{21}: Relative error [-]

h : Planck's constant [J s]

h_0 : Grid size [-]

$h_{g\text{-}s}$: Catalyst-gas heat transfer coefficient [$W\ m^{-2}\ K^{-1}$]

I: Identity matrix

$I_{exit,\ inlet}$: Light intensity [W]

k: Thermal conductivity [$J\ s^{-1}\ m^{-1}\ K^{-1}$]

k_b : Boltzmann's constant [$J\ K^{-1}$]

$k_{1,2}$: Rate constant [s^{-1}]

k_3: Rate constant [$m^3\ mol^{-1}s^{-1}$]

k_c: catalyst particle-gas mass transfer coefficient [$m\ s^{-1}$]

K_c: Chemical equilibrium constant [-]

k_d: Rate constant of the deactivation reaction [$m^3\ mol^{-1}s^{-1}$]

l : Optical path length

N : Number of cells [-]

p: Static pressure [Pa]

P; Static pressure [m]

Q_i: Temperature-dependant partition function of water vapour [-]

r: Reaction rate [mol m^{-3} s^{-1}]

R: Universal gas constant [J $mol^{-1}.K^{-1}$]

r_d: Reaction rate of deactivation [s^{-1}]

r_{21} : Refinement factor [-]

Re: Reynolds number [-]

r_p: Average pore radius

S : Line strength of temperature-dependent transition, [cm^{-2} atm^{-1}]

Sc: Schmidt number [-]

T: Temperature [K]

T_{ext} : Temperature of the surrounding medium [K]

u_s : fluid flow superficial velocity [m s^{-1}]

V_s: Volume of catalyst particle [m^3]

z: Axial coordinate of 1D model [m]

Greek symbols

ε: Porosity of catalyst particle [-]

ε_a : absorption coefficient [m^2 mol^{-1}]

ϕ : PBR porosity [-]

μ: Dynamic molecular viscosity [Pa s]

ρ: Density [kg m^{-3}]

ΔH_R: Enthalpy of reaction [J mol^{-1}]

ΔV: Cell volume [m^3]

u: Velocity vector [m s^{-1}]

τ: : Tortuosity [-]

λ: Wave length [nm]

Abbreviations

WGS: Water-gas-shift

PBR: Packed bed reactor

DEM: Discrete element method

PROX: preferential oxidation

NIR: Near-infrared

AR: Aspect ratio of tube to particle diameters

GCI: Grid Convergence Index

***Subscripts*:**

g: gaseous phase

s: solid phase

Surf : surface

Supporting materials:


mov1.avi


mov2.avi


mov3.avi

References

(1) S. Walke, S. Kambale, Catalyst Deactivation and Regeneration, International Journal of Scientific Engineering and Technology 4 (2015) 281-285

(2) J.D Grunwaldt, J. B. Wagner, R.E. Dunin-Borkowski, Imaging Catalysts at Work: A Hierarchical Approach from the Macro- to the Meso- and Nano-scale, ChemCatChem 5 (2013) 62-80

(3) E.Petersen, Catalyst deactivation: Opportunity amidst woe, Studies in Surface Science and Catalysis 111 (1997) 87-98

(4) H. Freund, J. Bauer, T. Zeiser, G. Emig, Detailed simulation of transport processes in fixed-beds, Industrial Engineering Chemistry Research 44 (2005) 6423− 6434

(5) C.O. Castillo-Araiza, F. López-Isunza, The role of catalyst activity on the steady state and transient behavior of an industrial-scale fixed bed catalytic reactor for the partial oxidation of o-xylene on V_2O_5/TiO_2 catalysts, Chemical Engineering Journal 176-177 (2011) 26–32

(6) G.D. Wehinger, T. Eppinger, M. Kraume, Detailed numerical simulations of catalytic fixed-bed reactors: Heterogeneous dry reforming of methane, Chemical Engineering Science 12 (2015) 197–209

(7) G.C. Lopes, L.M. Rosa, M. Mori, J.R. Nunheza, W.P. Martignoni, Three-dimensional modeling of fluid catalytic cracking industrial riser flow and reactions. Computers and Chemical Engineering 35 (2011) 2159– 2168

(8) G. Wang, F. Wang, L. Li, G. Zhang, Experimental investigation of axially non-uniform catalysis for methanol steam reforming, Journal of Power Sources 250 (2014) 306-312

(9) Y.S. Cheng, C.F. Abi, L.S. Kershenbaum, Estimation for a fixed-bed reactor with catalyst deactivation using nonlinear programming techniques, Comp. Chem. Eng. 20 (1996) 793-798

(10) A.I. Anastasov, Deactivation of an industrial V_2O_5-TiO_2 catalyst for oxidation of oxylene into phthalic anhydride, Chemical Engineering and Processing 42 (2003) 449-460

(11) G. Hofmann, A Rochet, S. Baier, M. Casapu, S. Ritter, F. Wilde, M. Ogurreck, F. Beckmann, G.D. Grunwaldt, Ageing effects on exhaust gas catalysts: microscopic changes captured by X-ray tomography, 22nd International Congress on X-Ray Optics and Microanalysis, Journal of Physics: Conference Series 499 (2014) 012017

(12) A. Devaraj, M. Vijayakumar, J. Bao, M.F. Guo, M.A Derewinski, Z. Xu, J.M. Gray, S. Prodinger, K.K. Ramasamy, Discerning the Location and Nature of Coke Deposition from Surface to Bulk of Spent Zeolite Catalysts, Scientific reports 6 (2016) 37586

(13) Y.M. Chunga, D. Mores, B.M. Weckhuysen, Spatial and temporal mapping of coke formation during paraffin and olefin aromatization in individual H-ZSM-5 crystals, Applied Catalysis A: General 404 (2011) 12–20

(14) S.I. Sanchez, M.D. Moser, S.A. Bradley, Mechanistic Study of Pt−Re/γ-Al2O3 Catalyst Deactivation by Chemical Imaging of Carbonaceous Deposits Using Advanced X-ray Detection in Scanning Transmission Electron Microscopy, ACS Catal. 4 (2014) 220−228

(15) F. Aiouache, H. Oyama, K. Kitagawa, Spatial Near-Infrared Imaging of Hydroxyl Band Coverage on Ceria-Based Catalysts, AIChE Journal 52 (2006) 1516-1521

(16) M.N. tSaoir, D.L.A. Fernandes, J. Sá, M. McMaster, K. Kitagawa, C. Hardacre, F. Aiouache, Transient distributions of composition and temperature in a gas–solid PBR by near-infrared tomography, Chemical Engineering Journal 189– 190 (2012) 383– 392

(17) M.N. tSaoir, D.L.A. Fernandes, J. Sá, M. McMaster, K. Kitagawa, C. Hardacre, F. Aiouache, Visualization of H2OV flow in a packed bed adsorber by near-infrared diffused transmittance tomography. Chem. Eng. Scien. 66 (2011) 6407–6423

(18) F. Aiouache, Imaging Gas Flow in Gas-Solid Catalytic Systems by Near-Infrared Tomography, Spatially Resolved Operando Measurements in Heterogeneous Catalytic Reactors. Spatially Resolved Operando Measurements in Heterogeneous Catalytic Reactors, A. Dixon and O. Deutschmann, Academic press 50(2017) 203-280

(19) K. Liu, A. Wang, T. Zhang, Recent Advances in Preferential Oxidation of CO Reaction over Platinum Group Metal Catalysts, ACS Catal. 2 (2012) 1165−1178

(20) A. Sirijaruphan, J.D. Goodwin Jr, R.W. Rice, Investigation of the initial rapid deactivation of platinum catalysts during the selective oxidation of carbon monoxide, Journal of Catalysis 221 (2004) 288–293
(21) A. Sirijaruphan, R.W. Goodwin Jr, R.W. Rice, Effect of Fe promotion on the surface reaction parameters of Pt/γ -Al_2O_3 for the selective oxidation of CO, J. of Catal. 224 (2004) 304–313
(22) L.S.Rothman, I.E.Gordon, A. Barbe, D. Chris Benner,P.F. Bernath, M. Birk, V. Boudon, L.R. Brown, A. Campargue, A. J.-P. Champion, K. Chance, L.H. Coudert, V. Dana, V.M. Devi, S. Fally, J.-M. Flaud, R. Gamache, A. Goldman, D. Jacquemart, I. Kleiner, N. Lacome, W.J. Lafferty, Y.-J. Mandin, S.T. Massie, S.N. Mikhailenko, C.E. Miller, N. Moazzen-Ahmadi, O.V. Naumenko, A.V. Nikitin, J. Orphal,V.I. Perevalov, A. Perrin, A. Predoi-Cross, C.P. Rinsland, M. Rotger, M. Simeˇkova, M.A.H. Smith, K. Sung, S.A. Tashkun, J. Tennyson, J.; R.A. Toth, A.C. Vandaele, J. Vander Auwera, The HITRAN 2008 molecular spectro-scopic database. J. Quant. Spectrosc. Radiat. Transfer 110 (2009) 533–572.
(23) T.A. Semelsberger, R.L. Borup, Fuel effects on start-up energy and efficiency for automotive PEM fuel cell systems, International Journal of Hydrogen Energy 30 (2005) 425-435
(24) M. Sun, E.B. Croiset, R.R. Hudgins, P.L. Silveston, Steady-State Multiplicity and Superadiabatic Extinction Waves in the Oxidation of CO/H_2 Mixtures over a Pt/Al_2O_3-Coated Monolith, Ind. Eng. Chem. Res. 42 (2003) 37-45,
(25) N. Rankovic, A. Nicolle, D. Berthout, P. Da Costa, Kinetic modeling study of the oxidation of carbon monoxide hydrogen mixtures over Pt/Al_2O_3 and Rh/Al_2O_3 catalysts, J. Phys. Chem. C, 115 (2011) 20225–20236
(26) M.J. Castaldi, R. LaPierre, M. Lyubovski, W. Pfefferle, S. Roychoudhury, Effect of water on performance and sizing of fuel-processing reactors, Catalysis Today 99 (2005) 339–3
(27) D.H. Kim, M.S. Lim, Kinetics of selective CO oxidation in hydrogen rich mixtures on Pt/alumina catalysts, Appl Catal A. 224 (2002) 27-38.
(28) X. Ouyang, L. Bednarova, R.S. Besser, Preferential oxidation (PrOx) in a thin-film catalytic microreactor : advantages and limitations, AIChE Journal 51 (2005) 1758-1772
(29) J.C. Amphlett, R.F. Mann, B.A. Peppley, On board hydrogen purification for steam reformation/ PEM fuel cell vehicle power plants, Int. J. Hydrogen Energy 21 (1996) 673–678
(30) Y. Choi, H.G. Stenger, Kinetics, simulation and insights for CO selective oxidation in fuel cell applications, Journal of Power Sources 129 (2004) 246–254
(31) A. Jaree, R.R. Hudgins, H.M. Budman, P.L. Silveston, Hysteresis and Extinction Waves in Catalytic CO Oxidation Caused by Reactant Concentration Perturbations in a PBR, Ind. Eng. Chem. Res. 42 (2003) 1662-1673
(32) T. Engel, G.Ertl, Elementary Steps in the Catalytic Oxidation of Carbon Monoxide on Platinum Metals, Adv. Catal. 28 (1979) 1-78
(33) S. Szépe, O. Levenspiel, Catalyst deactivation, in: Proceedings of the fourth European Symposium on Chemical Reaction Engineering, Pergamon Press, NY (1971) 265–276.
(34) S. Szépe, O. Levenspiel, ptimal temperature policies for reactors subject to catalyst deactivation-I batch reactor, Chemical Engineering Science 23 (1968) 881-894
(35) J. Stewart, R. Douglas, A. Goguet, C. Stere, Detailed validation of an automotive catalysis model using spatially resolved measurements within the catalyst substrate, The Canadian Journal of Chemical Engineering 92 (2014) 1535-1541
(36) C.N. Montreuil, S.C. Williams, A.A. Adamczyk, Modeling current generation catalytic converters: laboratory experiments and kinetic parameter optimization-Steady state kinetics, Warrendale, Penn: Society of Automotive Engineers (1992) SAE paper 920096
(37) A.G. Dixon, M.E. Taskin, M. Nijemeisland, E.H. Stitt, CFD Method to couple three-dimensional transport and reaction inside catalyst particles to the fixed bed flow field. Industrial & Engineering Chemistry Research 49 (2010) 9012-9025.
(38) A. Jaree, B. Boonsomlanjit, J. Limtrakul, On the dynamical instability of PBRs in the presence of catalyst deactivation, Computers and Chemical Engineering 32 (2008) 2897–2902

(39) M. Giese, M. Rottschaffer, D. Vortmeyer, Measured and modelled superficialflow profiles in packed beds with liquid flow, AIChE J. 44 (1998) 484–490.
(40) R.P. Zou, A.B. Yu, The packing of spheres in a cylindrical container: The thickness effect. Chem. Eng. Sci. 50 (1995) 1504-1507.
(41) K.F. Jensen, W.H. Ray, The bifurcation behavior of tubular reactors, Chemical Engineering Science 37 (1982) 199-222
(42) R.C. Reid, J.M. Praunitz, B.E. Poling, The Properties of Gases and Liquids, 4th ed. McGraw-Hill 1987
(43) M.M. Tomadakis, S.V. Sotirchos, Transport properties of random arrays of freely overlapping cylinders with various orientation distributions, J. Chem. Phys. 98 (1993) 616-626.
(44) I.B. Celik, U. Ghia, P.J. Roache, C.J. Freitas, H. Coleman, P.E. Raad, Procedure for estimation and reporting of uncertainty due to discretization in cfd applications, J. Fluids Eng. 130 (2008) 078001
(45) F. Alzahrani, M. Aldehani, H. Rusi, M. McMaster, D.L.A. Fernandes, S. Assabumrungrat, M.N. tSaoir, F. Aiouache, Gas flow visualization in low aspect ratio packed beds by three-dimensional modeling and near-infrared tomography. Industrial & Engineering Chemistry Research 64 (2015) 12714-12729
(46) A. Pachulski, R. Schodel, P. Claus, Kinetics and reactor modeling of a Pd-Ag/Al_2O_3 catalyst during selective hydrogenation of ethylene, Applied Catalysis A: General 445 (2012) 107– 120

APPENDIX A1

Light propagates through non-transparent media into ballistic, quasi-ballistic or diffuse light. The ballistic light follows a straight trajectory in the medium, the quasi-ballistic light carries out minor scattering, while the diffuse light goes through multiple scattering and directions.[16-18] The ballistic light therefore travels straight through a non-transparent medium and exits in a similar direction to that in which it entered, but constitutes typically a very small part of the light. The concentration of H_2O_V was obtained by measuring the attenuation of the light through the low scattering PBR, which included both absorption and some scattering and is described by the modified Beer–Lambert law.

$$Abs = \ln \frac{I_{exit}}{I_{inlet}} = -\varepsilon_a \left(T, \lambda\right) \int c_{H_2O_V} dl \qquad \text{(A.1.1)}$$

where Abs is the absorbance, I_{exit} and I_{inlet} are the light intensities at the exit and the inlet of the packed bed, respectively, l is the optical path length, c_{H2O} is the uneven composition of H_2O_V across the packing and ε_a is the absorption coefficient.

The temperature was measured by computing the ratio, R_{abs}, of integral absorbance Abs_1 and Abs_2 for two temperature-dependent wave lengths λ_1 and λ_1.[19]

$$R_{abs} = \frac{Abs_1(T,\lambda_1)}{Abs_2(T,\lambda_2)} \tag{A.1.2}$$

The values of the two integral absorbances were taken from the same interrogatory area in terms of concentration and path length. R_{abs} was then simplified to ratios of the absorption coefficient or line strength $S(T)$ of temperature-dependent transition:

$$R_{abs} = \frac{\varepsilon_1(T,\lambda_1)}{\varepsilon_2(T,\lambda_2)} = \frac{S_1(T,\lambda_1)}{S_2(T,\lambda_2)} \tag{A1.3}$$

The line strength at an arbitrary temperature T is related to a reference temperature T_0 as given by Equation (A.1.4).

$$S_i(T) = S_i(T_0)\frac{Q_i(T_0)}{Q_i(T)}\left(\frac{T_0}{T}\right)\exp\left[-\frac{hcE_i}{k_b}\left(\frac{1}{T}-\frac{1}{T_0}\right)\right]\frac{\left[1-\exp\left(-\frac{hc_0}{kT\lambda_0}\right)\right]}{\left[1-\exp\left(-\frac{hc_0}{kT_0\lambda_0}\right)\right]} \tag{A.1.4}$$

$Q_i(T)$ is the temperature-dependent partition function of water vapour, $S_i(T_0, \lambda_i)$ is the line strength of the transition centred at line wavelength λ_i for a reference temperature T_0, often taken as 296 K, h is Planck's constant, c is the speed of light, k is Boltzmann's constant and E_i is the lower state energy. The absorbance ratio is thus related to temperature by Equation (A.1.5).

$$R = \frac{S_1(T_0)}{S_2(T_0)}\exp\left[-\frac{hc(E_1-E_2)}{k_b}\left(\frac{1}{T}-\frac{1}{T_0}\right)\right]\frac{\left[1-\exp\left(-\frac{hc}{kT\lambda_1}\right)\right]}{\left[1-\exp\left(-\frac{hc}{kT\lambda_2}\right)\right]} \tag{A.1.5}$$

The pair of lines at 1358.412 and 1380.685 nm were used for temperature measurements since they offered a difference in lower state energy (E_2-E_1) of 342 cm^{-1}, a line strength ratio at the reference temperature ($S_1(T_0)/S_2(T_0)$) of 1.19, and were close but not overlapping each other.

The adaptive algebraic reconstruction technique was employed for image reconstruction of both temperature and concentration measurements, as it offered flexibility for a reduced number of projections. The 3D object function *f*, of dimension m *and N,* represented an array of discrete unknown voxels. For a single hyperplan, integral absorbance (equation A.1.1) or integral ratio of absorbance (equation A.1.5) for concentration and temperature measurements, respectively, along the path were expressed by equation A.1.6.

$$\sum_{j=1}^{M} w_{ij} f_i = p_i \qquad i = 1,2,..N \qquad (A.1.6)$$

Where p is the integral absorbance or absorbance ratio, w_{ij} is the weighting factor, representing absorbance (i.e. concentration) or absorbance ratio (i,e, temperature) of the contribution of the j-th voxel to the i-th measurement, N is the total number of projection rays and M is the total number of voxels. The algorithm was initiated by giving an arbitrary guess for the voxel vector, projecting onto the first hyperplan equation and the result was projected onto the next hyperplan and so on until the last one. The system of algebraic equations was solved by iteration using the Kaczmarz method (equation A.1.7).

$$f_j^l = f_j^{l-1} - \frac{f_j^{l-1}.w_{ij}}{\sum_{j=1}^{N} w_{ij}.\left(f_j^{l-1}.w_{ij}\right)}\left(\sum_{j=1}^{N} w_{ij} f_j^{l-1} - p_i\right) \qquad (A.1.7)$$

where $f^{k-1}.w_i$ is the dot product and k is the iteration index. Reconstruction of cross-sectional images or slice matrixes was repeated for each subsequent cross-sectional matrix until 3D integral absorbance ratios for temperature reconstructions and integral absorbance for concentration reconstructions were obtained and converted to temperature and concentration using equations A.1.1 and A.1.5, respectively.

APPENDIX A2

The Weisz and Prater (W–P) criterion (Equation A.2.1) and Mears criterion (Equation A.2.2) were used to assess the relative effects of internal and external mass transfer limitations, respectively, on the chemical kinetics. A negligible mass transfer limitation takes place when the two factors in Equations A.2.1 and A.2.2 are satisfied.[27,28]

$$W-P=\left|\frac{r_i d^2}{4D_{i,s}c_{i,suf}}\right|<0.3 \tag{A.2.1}$$

$$Mears=\left|\frac{r_i d}{k_c c_{i,g}}\right|<0.3 \tag{A.2.2}$$

Herein, k_c is the mass transfer coefficient relevant to the film surrounding a spherical particle, which was estimated from the model of films surrounding spheres.[46]

$$\frac{k_c d}{D_{i,s}}=0.692\,\mathrm{Re}^{0.514}\,Sc^{0.33} \tag{A.2.3}$$

The concentration on the surface of the catalyst $c_{i,sur}$ was obtained by mass balance at the gas–solid boundary.

$$r_i V_s=k_c a_s\left(c_{i,g}-c_{i,surf}\right) \tag{A.2.4}$$

where a_s and V_s are the surface area and volume of a single particle, respectively.

The criteria of the Damköhler numbers in 4th order $Da_{i,(IV)}$ (Equation A.2.5) and 3rd order $Da_{i,(III)}$ (Equation A.2.6) were used to assess the relative effects of internal and external heat transfer limitations, respectively, on the chemical kinetics. Herein, the enthalpy of reaction ΔH_{rj} and activation energy E_j are those relevant to CO oxidation in the PROX.

$$Da_{i(IV)}=\left|\frac{-\Delta H_{rj} r_i d^2}{4k_c T_s}\right|<\frac{0.4RT_{surf}}{E_j} \tag{A.2.5}$$

$$Da_{i(III)}=\left|\frac{-\Delta H_{rj} r_i d}{2h_{g-s} T_g}\right|<\frac{0.15RT_g}{E_j} \tag{A.2.6}$$

where R is the universal gas constant and $h_{g\text{-}s}$ is the heat transfer coefficient from the gas phase to the catalyst and was estimated from the model of films surrounding spheres.[46]

$$\frac{h_{g-s}d}{k_g}=\frac{1.192\left(1-\varepsilon\right)^{0.41}Re\,Pr^{0.33}}{Re^{0.41}-1.52\left(1-\varepsilon\right)^{0.41}} \tag{A.2.7}$$

Re and *Pr* are the dimensionaless Reynolds and Prandtl numbers, respectively. The surface catalyst temperature T_{surf} was obtained by the heat balance at the gas–solid boundary.

$$\Delta H_{rj}r_iV_s=h_{g-s}a_s\left(T_{suf}-T_g\right) \tag{A.2.8}$$

APPENDIX A3

Potential errors that could be associated with the CFD simulation were examined by following the approach given by Celik et al.,[44] ensuring that the results were free of mesh size. The representative grid size h_0 procedure was defined as:

$$h_0=\left(\frac{1}{N}\sum_{i=1}^{N}\Delta V_i\right)^{1/3} \tag{A.3.1}$$

where ΔV is the cell volume and N is the number of cells. Three grid refinement factors higher than 1.3 were used for the ultimate refinements. The apparent order *m* of the method was defined by Equations (A.3.2) to (A.3.4.) :

$$m=\left|\ln\left|\Theta_{32}/\Theta_{21}\right|+q\left(m\right)\right|/\ln\left(r_{21}\right) \tag{A.3.2}$$

$$q\left(m\right)=\ln\left(\frac{r_{21}^{m}-s}{r_{32}^{m}-s}\right) \tag{A.3.3}$$

$$s=1.\mathrm{sgn}\left(\Theta_{32}/\Theta_{21}\right) \tag{A.3.4}$$

where $h_{0,1}<h_{0,2}<h_{0,3}$, $r_{21}=h_{0,2}/h_{0,1}$, $r_{32}=h_{0,3}/h_{0,2}$, $\Theta_{32}=u_3-u_2$, $\Theta_{21}=u_2-u_1$. u_k(k=1, 2, 3) expresses velocity values taken at three grid locations in the packed bed as shown in **Figure A.3** and sgn is the function

signum. Equation (A.3.3) was solved numerically for *m*. This was used to find the relative errors (Equations A.3.5 and A.3.6) and the fine grid convergence GCI (Equations A.3.7 and A.3.8)

$$e_a^{21} = \frac{u_1 - u_2}{u_1} \tag{A.3.5}$$

$$e_a^{32} = \frac{u_2 - u_3}{u_2} \tag{A.3.6}$$

$$GCI^{21} = \frac{1.25 e_a^{21}}{r_{21}^m - 1} \tag{A.3.7}$$

$$GCI^{32} = \frac{1.25 e_a^{32}}{r_{32}^m - 1} \tag{A.3.8}$$

Table 1. Physical properties of gaseous and packing phases*

Gaseous phase		
Property	N_2	He
ρ_g [kg m^{-3}]**	0.68	0.1
μ_g [Pa s]**	2.63 x 10^{-5}	2.89 x 10^{-5}
$k_g(js^{-1}m^{-1}K^{-1})$**	$k_g = 6.0 \times 10^{-5}T(℃) + 0.0247$	$k_g = 3.0 \times 10^{-4}T(℃) + 0.1504$
C_{pg} [J kg^{-1} K^{-1}]**	1021.2	5193.2
$D_{i\text{-}x}$ [m^2 s^{-1}] (x: N_2 or He)***	$D_{H_2O-N_2} = 1.7 \times 10^{-7}T(℃) - 3.3 \times 10^{-5}$ $D_{H_2-N_2} = 4.8 \times 10^{-7}T(℃) - 9.9 \times 10^{-5}$ $D_{CO-N_2} = 1.5 \times 10^{-7}T(℃) - 2.8 \times 10^{-5}$ $D_{CO_2-N_2} = 1.1 \times 10^{-7}T(℃) - 1.8 \times 10^{-5}$ $D_{O_2-N_2} = 1.5 \times 10^{-7}T(℃) - 2.6 \times 10^{-5}$	$D_{H_2O-He} = 4.7 \times 10^{-7}T(℃) - 8.4 \times 10^{-5}$ $D_{H_2-He} = 8.5 \times 10^{-7}T(℃) - 1.6 \times 10^{-4}$ $D_{CO-He} = 4.3 \times 10^{-7}T(℃) - 7.5 \times 10^{-5}$ $D_{CO_2-He} = 3.8 \times 10^{-7}T(℃) - 6.6 \times 10^{-5}$ $D_{O_2-He} = 4.5 \times 10^{-7}T(℃) - 7.5 \times 10^{-5}$
Solid phase (Pt/γ-Al_2O_3)		
ρ_s [kg m^{-3}]	1230	
ε_s [-]	0.21	
τ_s****	2.15 [43]*	
Surface area [m^2 g^{-1}]	218	
k_s (J s^{-1} m^{-1} K^{-1})	27	
C_{ps} [J kg^{-1} K^{-1}]	880	

* The physical properties of the reactive mixture were predominantly approximated to that of the carrier gases owing to low concentrations of the reactive species. Some properties such as density and viscosity were averaged over the operating temperature (i.e. 413-650 K) to reduce the computation time of the 3D model.

**Data of physical properties were obtained from DIPPR models in Aspen Plus data base and then linearized into polynomial expressions (i.e. coefficient of determination $R^2 \geq 0.99$).

*** The model of Chapman-Enskog-Wilke-Lee was used [42]

****Tortuosity τ_s was estimated by the tortuosity-porosity model of Tomadakis et al.[43] where the pores are assumed to be structured of overlapping cylinders.

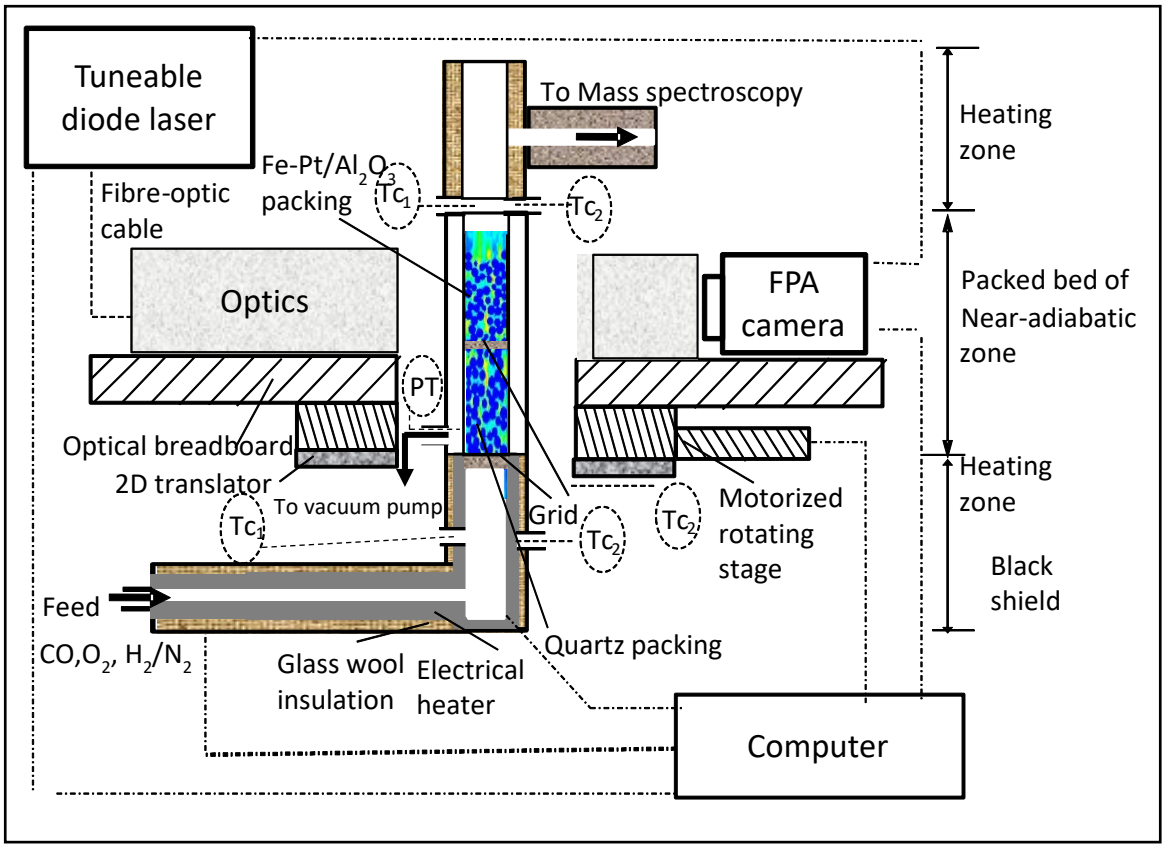

Figure 1 Apparatus scheme: Feed controlled by mass flow controller of CO, O_2, H_2 and N_2 and air-actuated switching valve for CO composition change, PT: Pressure transducer, TC_1= Thermocouples (monitoring), TC_2: Thermocouples connected to programmable temperature controllers; Optics=details of optics are shown in Figure 3; Tuneable diode laser: Lock-in monomode connected to focal planar camera; Quartz packing: pre-packed bed mixer, Fe-Pt/Al_2O_3 packed bed= Height: 39 mm; visible aperture by NIR camera: 1.20 x 3.9 cm^2

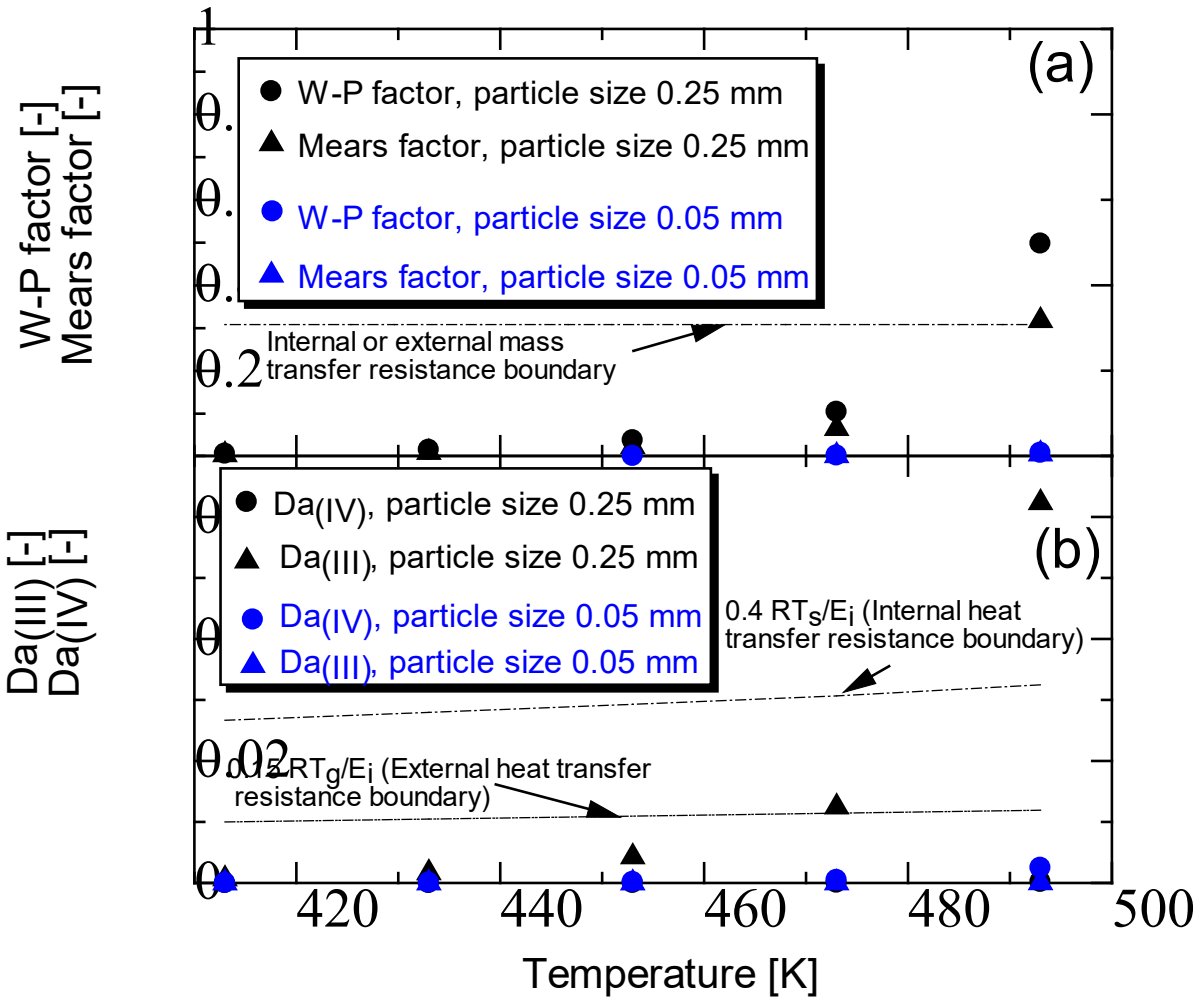

Figure 2 Profiles of W-P, Mears, $Da_{i,(IV)}$ and $Da_{i,(III)}$ factors with temperature for particle sizes of 250 μm (AR of 48) and 50 μm (AR of 240), feed flow rate of 670 cm^3 min^{-1} and composition: 0.5 mol% CO, 2.5 mol% O_2, 1.7 mol% H_2 and N_2 as carrier gas

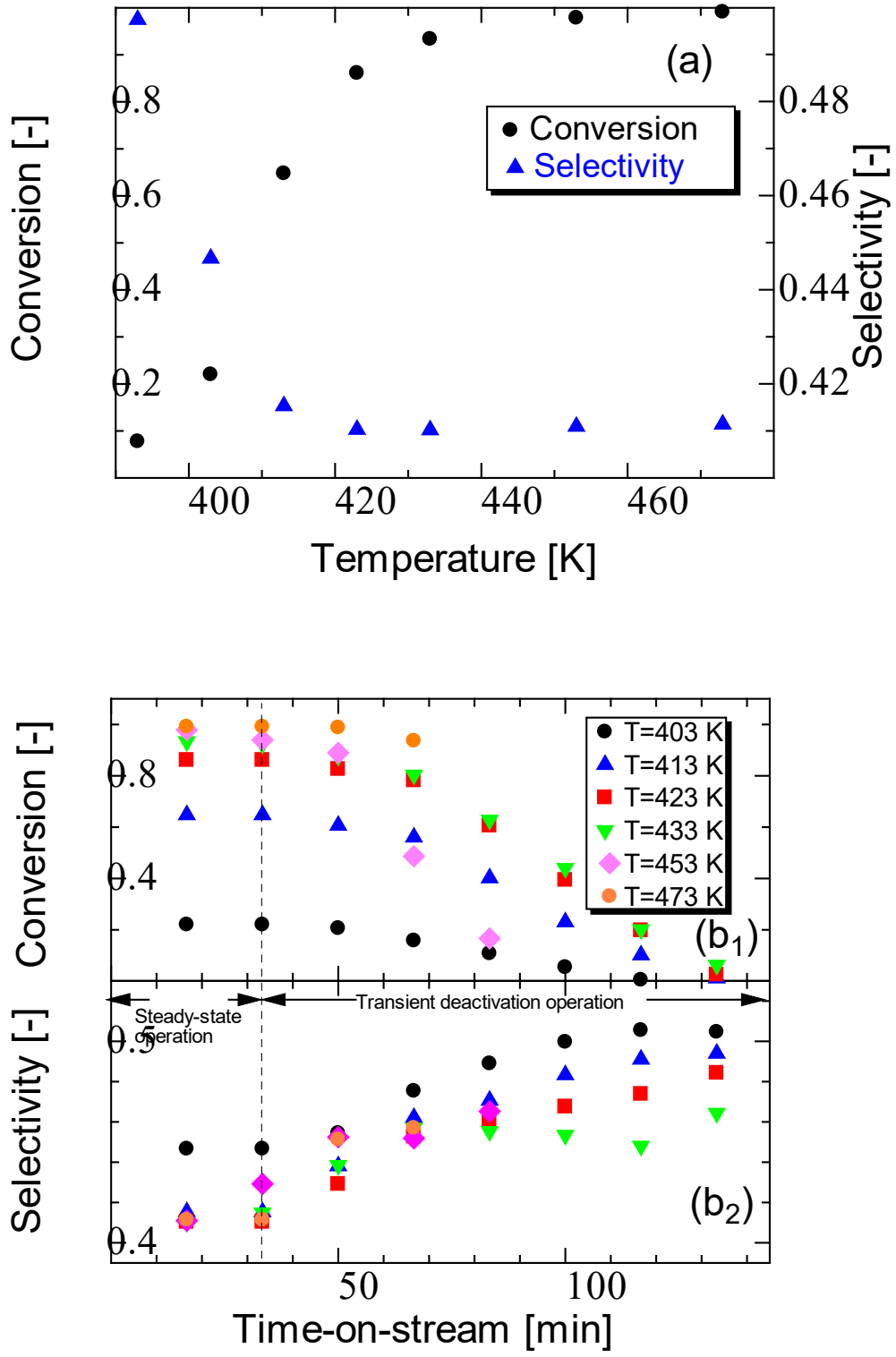

Figure 3 Profiles of conversion of CO and selectivity to CO_2 with temperature at steady-state conditions (a), profiles of conversion with time-on-stream and temperature (b1) and profiles of selectivity to CO_2 with time-on-stream and temperature (b2). PBR of an AR of 48 — i.e., particle size of 250 μm, feed flow rate of 670 cm^3 min^{-1} and composition: 0.5-1.1 mol% at steady-state and increased to 1.4% CO at transient conditions, 2.5 mol% O_2, 1.7 mol% H_2 and N_2 as carrier gas

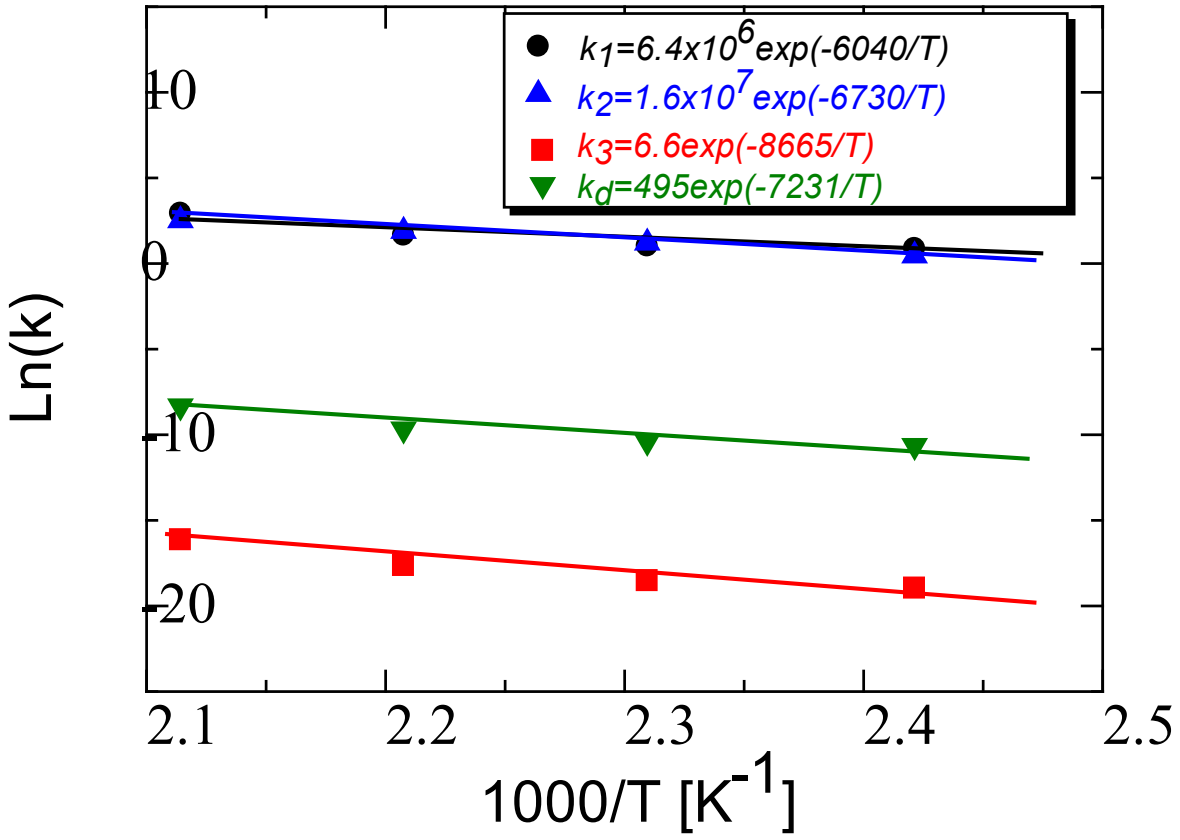

Figure 4 Profiles of rate constants with temperature. PBR of an AR of 48 — i.e., particle size of 0.25 mm, feed flow rate of 670 cm^3 min^{-1} and composition: 0.5-1.1 mol % at steady-state and increased to 1.4% CO at transient conditions, 2.5 mol% O_2, 1.7 mol% H_2 and N_2 as carrier gas

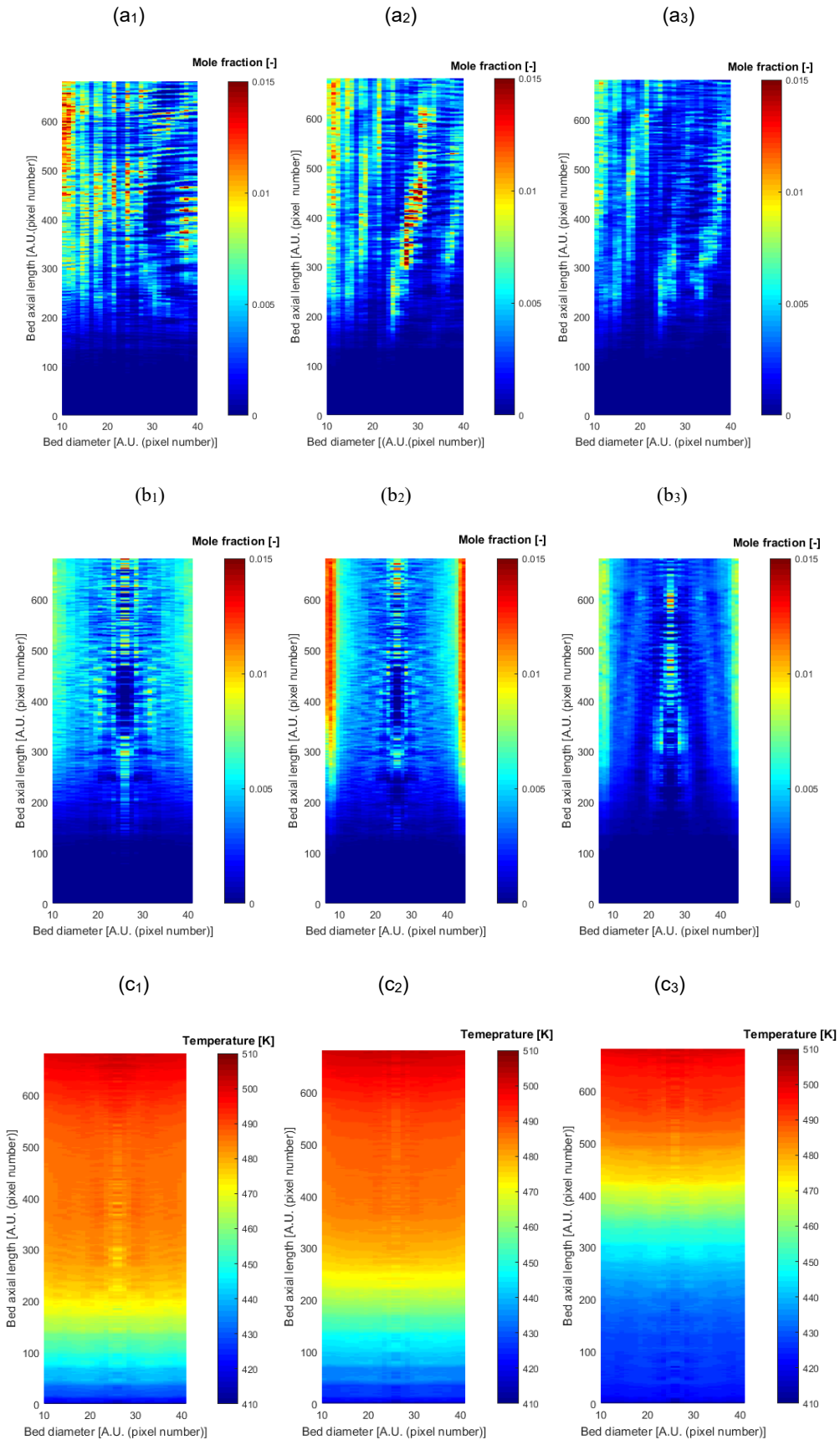

Figure 5 Axial section maps of concentration of H_2O_V (a_1-a_3), circumferentially averaged concentration maps of H_2O_V (b_1-b_3) and circumferentially averaged temperature maps (c_1-c_3). Subscripts 1, 2 and 3 correspond to times-on-stream of 30, 60 and 90 min, respectively, PBR of an AR of 13 — i.e., particle size of 0.9 mm, feed temperature of 413 K, flow rate of 670 cm^3 min^{-1}, and composition: 1.1 mol % at steady-state and increased to 1.4% CO at transient conditions, 2.5 mol% O_2, 1.7 mol% H_2 and N_2 as carrier gas

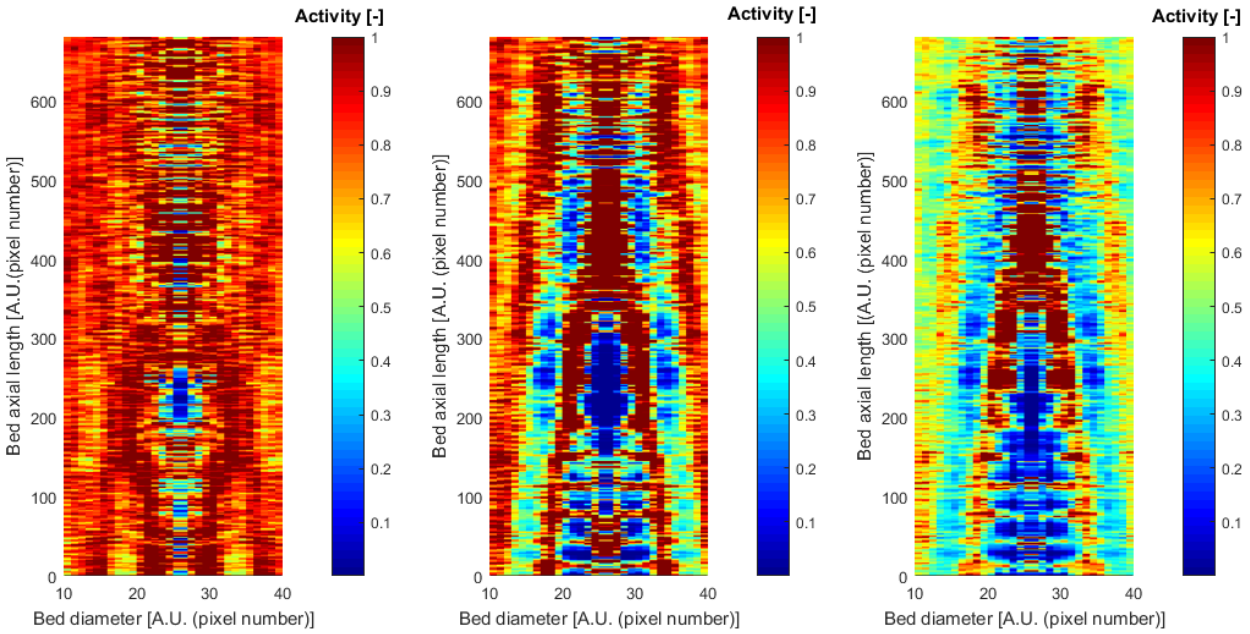

Figure 6 Circumferentially averaged local activity maps, (a), (b) and (c) correspond to times on stream of 30, 60 and 90 min, respectively, PBR of an AR of 13 — i.e., particle size of 0.9 mm, feed temperature of 413 K, flow rate of 670 cm^3 min^{-1}, and composition: 1.1 mol% at steady-state and increased to 1.4 mol% CO at transient conditions, 2.5 mol% O_2, 1.7 mol% H_2 and N_2 as carrier gas

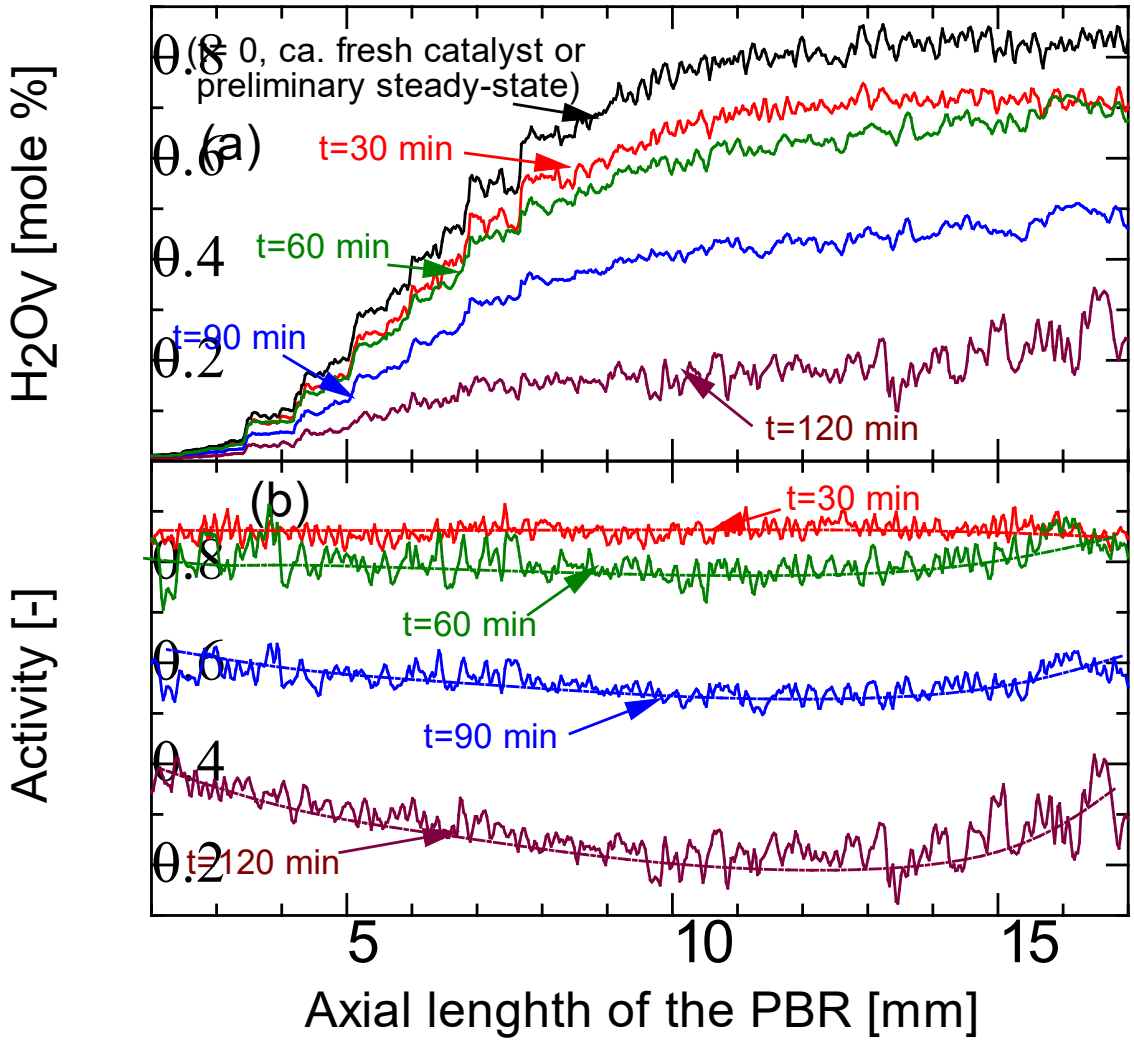

Figure 7 Circumferentially and radially averaged local concentration of H_2O_V (a) and activity (b) for times on stream of 30, 60, 90 and 120 min, respectively. PBR of an AR of 13 — i.e., particle size of 0.9 mm, feed temperature of 413 K, flow rate of 670 cm^3 min^{-1}, and composition: 1.1 mol% at steady-state and increased to 1.4 mol% CO at transient conditions, 2.5 mol% O_2, 1.7 mol% H_2 and N_2 as carrier gas

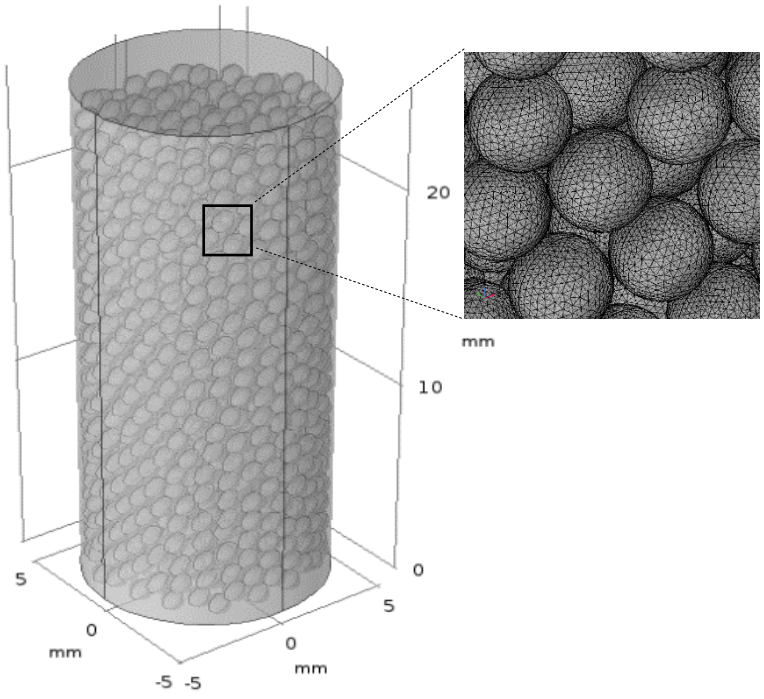

Figure 8 Elemental discretisation of catalyst particle by 3D unstructured tetrahedral cells (i.e. spatial resolution of 25 elements per particle diameter).

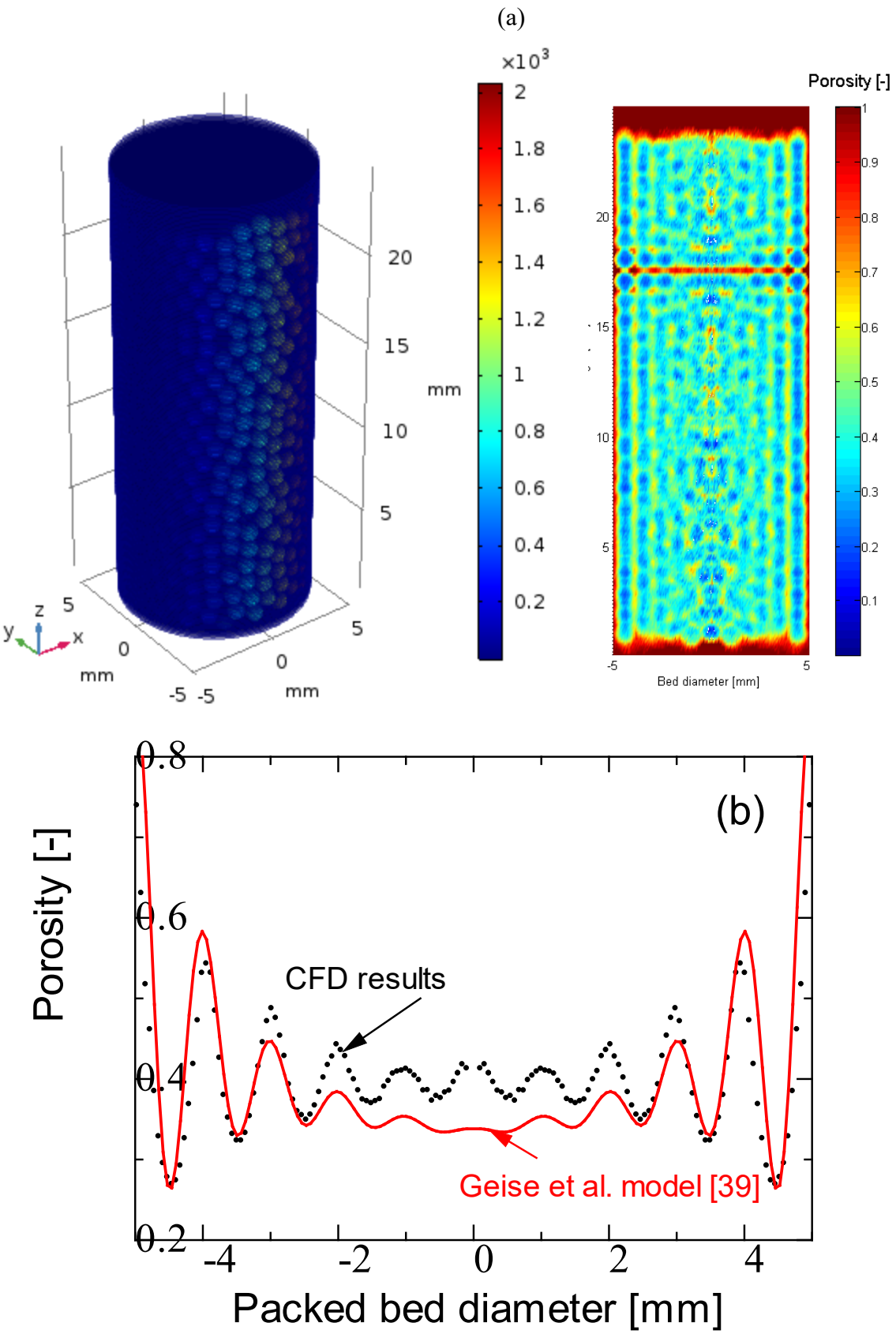

Figures 9 2D surface map (a) from circumferentially averaging the 3D domain index (left figure) and axial averaging of porosity (b)

(a)

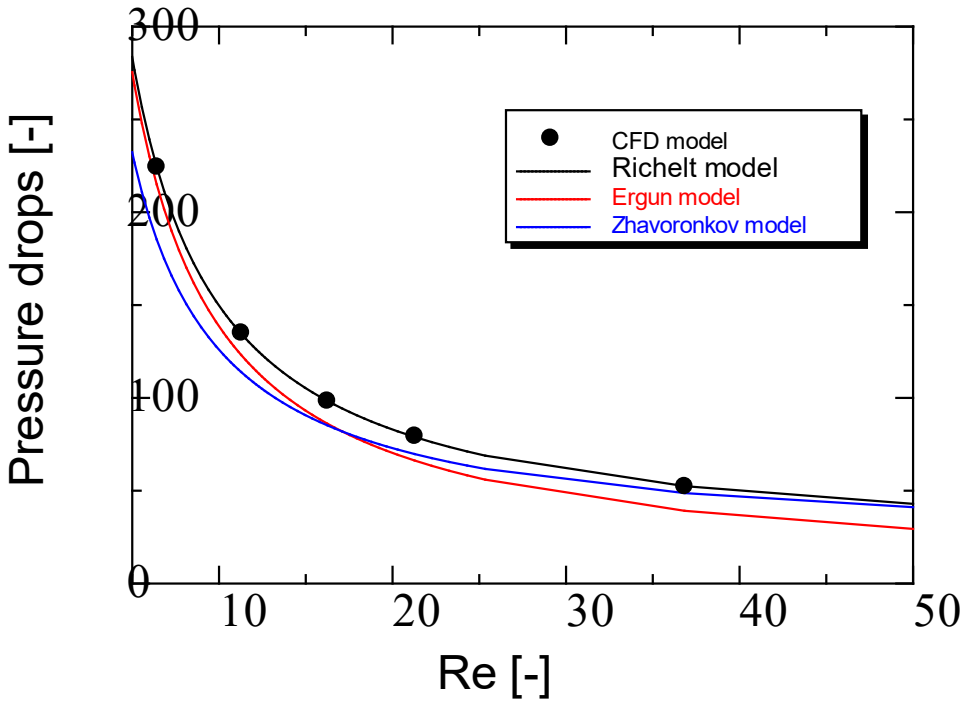
Pressure drops [-]
300
200
100
0
10
20
30
40
50
Re [-]
CFD model
Richelt model
Ergun model
Zhavoronkov model

(b)

(c)

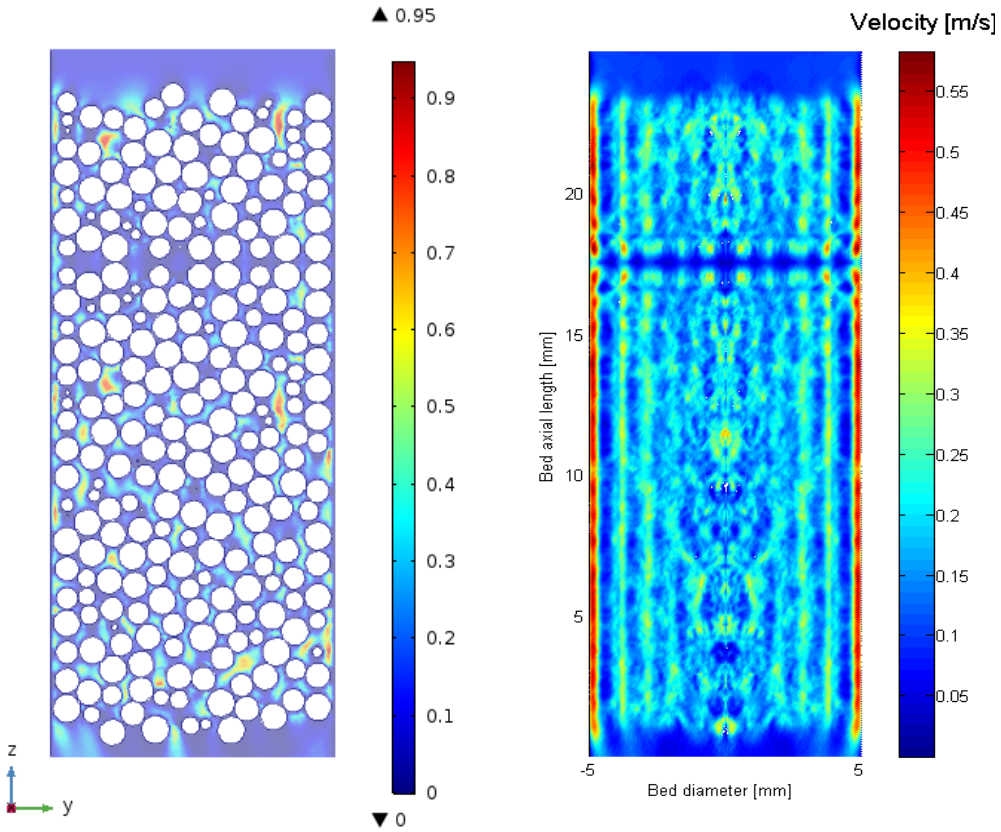
▲ 0.95
0.9
0.8
0.7
0.6
0.5
0.4
0.3
0.2
0.1
0
▼ 0
z
y
Velocity [m/s]
0.55
0.5
0.45
0.4
0.35
0.3
0.25
0.2
0.15
0.1
0.05
Bed axial length [mm]
20
15
10
5
-5
5
Bed diameter [mm]

(d_1)

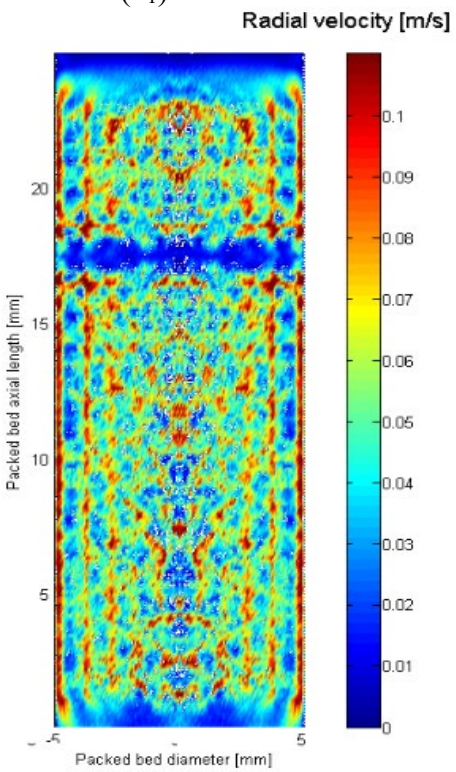

(d_2)

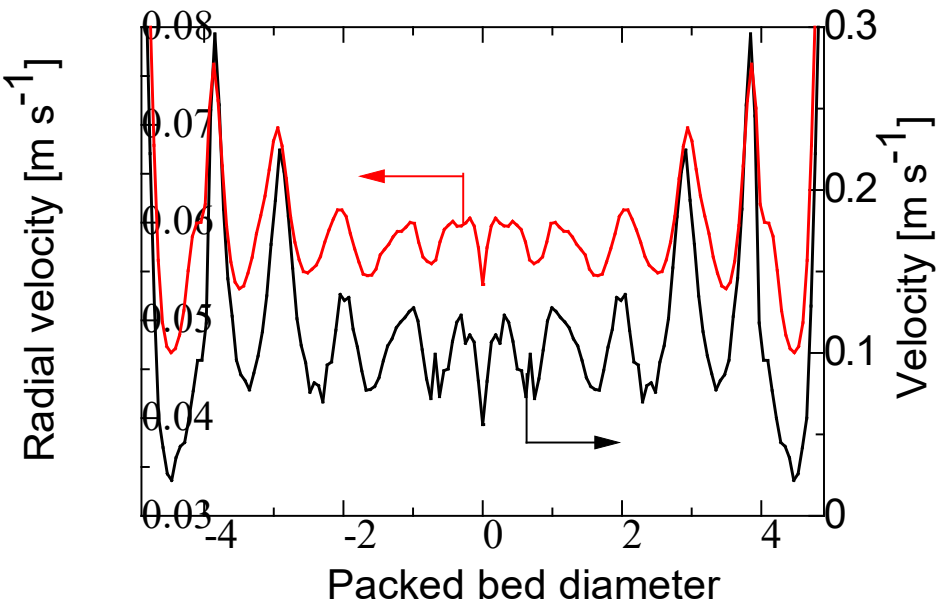

Figure 10 Pressure drops (a), vertical section map of velocity (b), circumferentially averaged map of velocity (c), circumferentially averaged radial velocity (d_1) and circumferentially and axially averaged radial velocity (d_2)

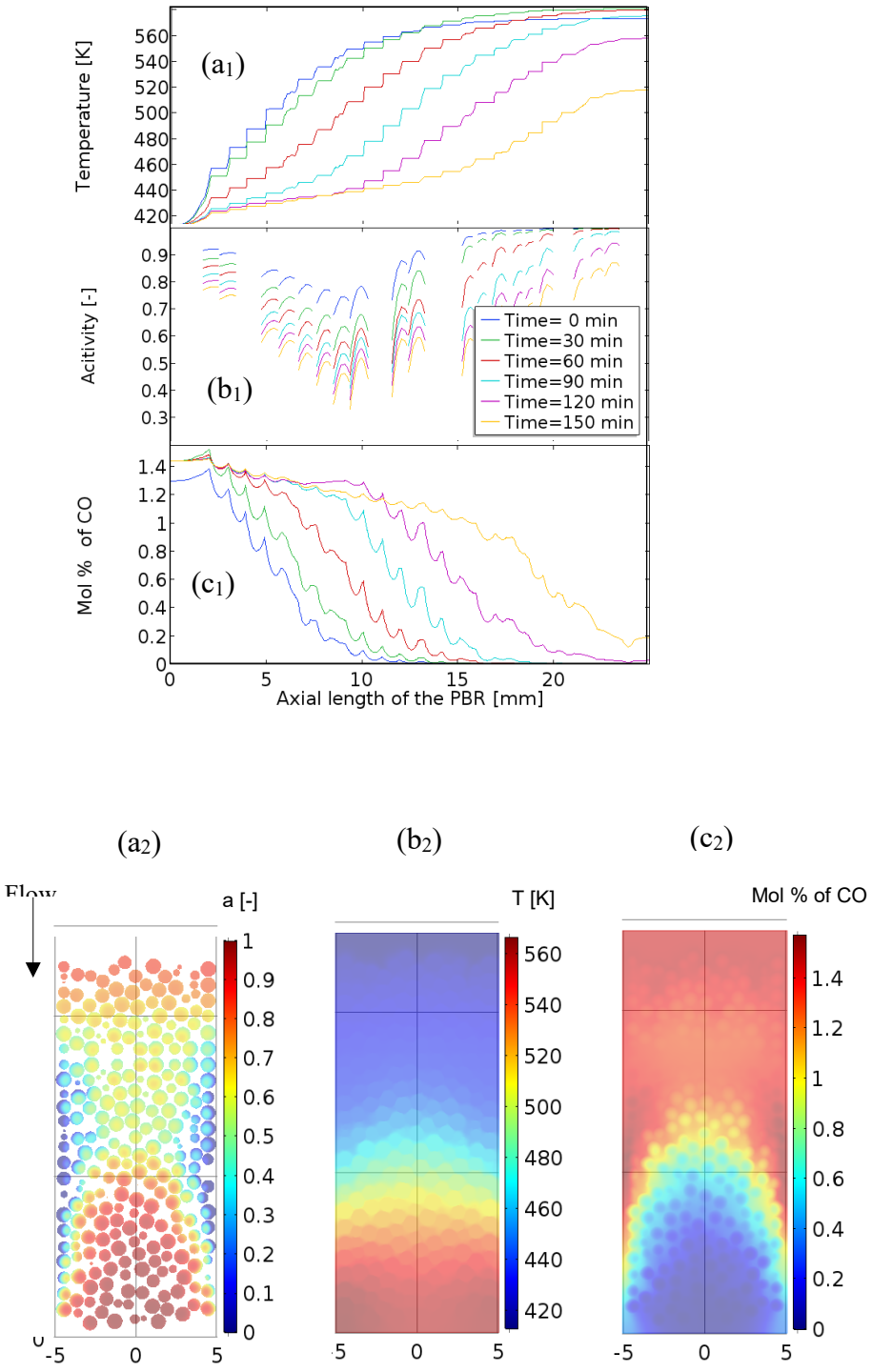

Figure 11 Profiles of axial cross-line of temperature (a_1), activity (b_1) and composition of CO (c_1) along the PBR at various time-on-stream, cross-sections at 120 min of time-on-stream of temperature (a_2), activity (b_2) and composition of CO (c_2), PBR of 10 mm ID, 25 mm length and AR of 10 — i.e., particle size of 1 mm, feed flow rate of 470 cm^3 min^{-1} and composition: 1.1 mol% at steady-state and increased to 1.4 mol% CO at transient conditions along with deactivation, 1.7 mol% H_2 and N_2 as carrier gas

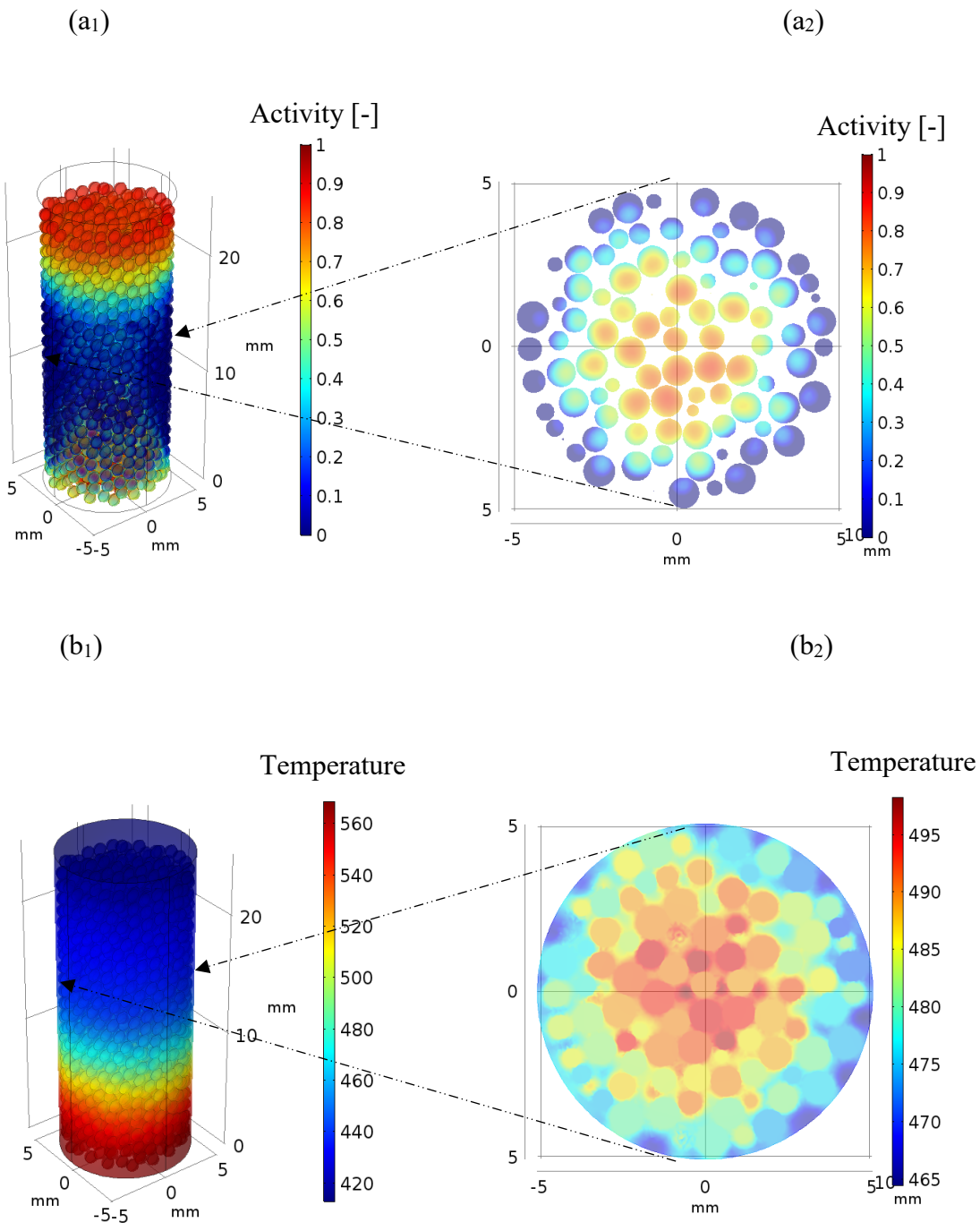

Figure 12 3D views and cross-sectional map of activity (a_1-a_2) and temperature (b_1-b_2) at time-on-stream of 120 min, cross-section at 15 mm from the inlet of the PBR, PBR of 10 mm ID, 25 mm length, particle size of 1 mm, feed flow rate of 470 cm^3 min^{-1} and composition: 1.1 mol% at steady-state and increased to 1.4 mol% CO at transient conditions along with deactivation, 1.7 mol% H_2 and N_2 as carrier gas

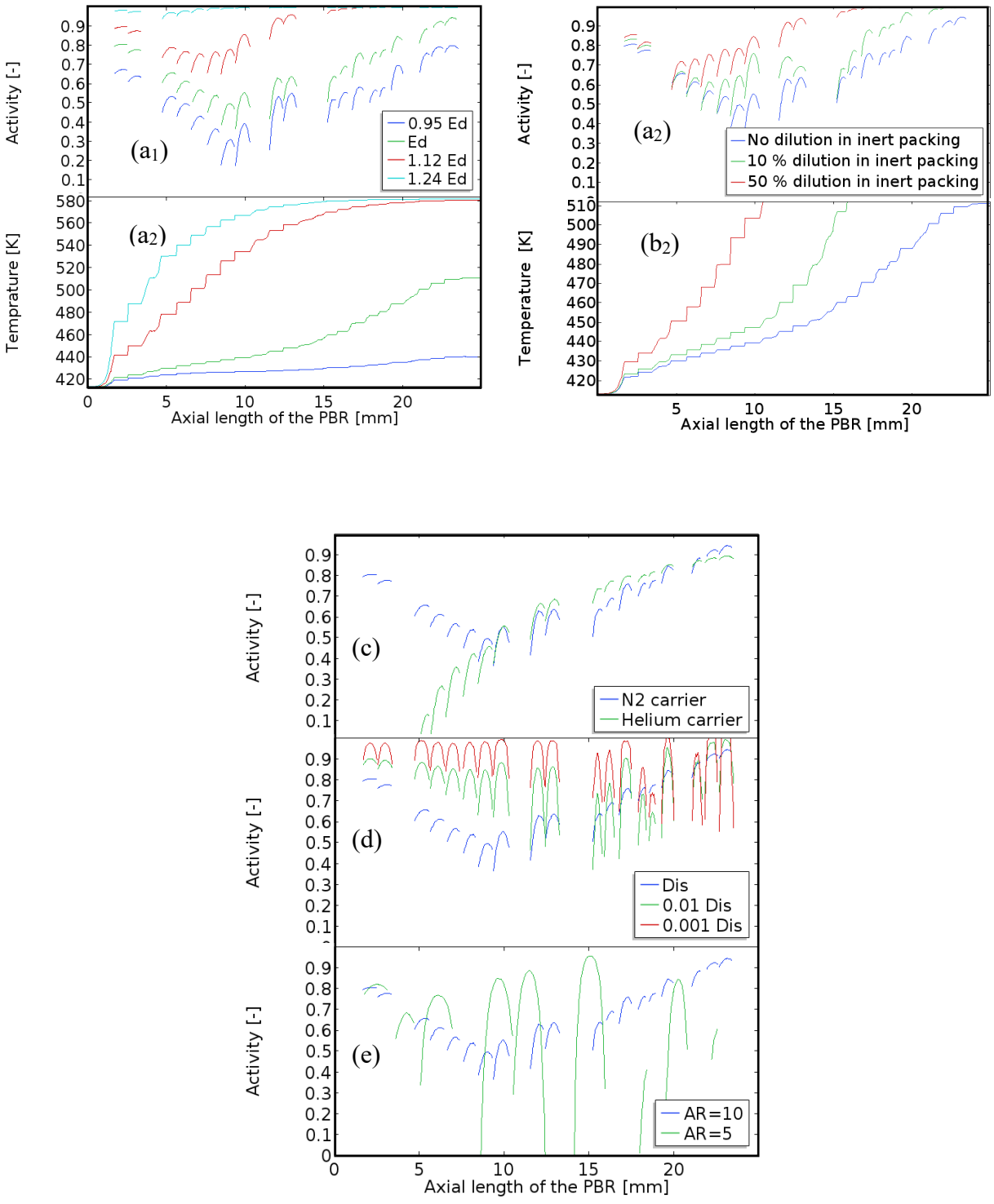

Figure 13 Profiles of axial cross-line of activity and temperature along the PBR at time-on-stream of 120 min. Effects of activation energy of deactivation rate constant on activity and temperature (a_1,a_2), dispersion of catalyst concentration on activity and temperature (b_1,b_2), mass and thermal diffusivity coefficients of carrier gas on activity (c) intra-particle mass transfer rate on activity (d) and The aspect ratio of bed to particle diameter on activity (e). PBR of 10 mm ID, 25 mm length, particle size of 1 mm, feed flow rate of 470 cm^3 min^{-1} and composition: 1.1 mol% at steady-state and increased to 1.4 mol% CO at transient conditions along with deactivation, 1.7 mol% H_2 and N_2 as carrier gas

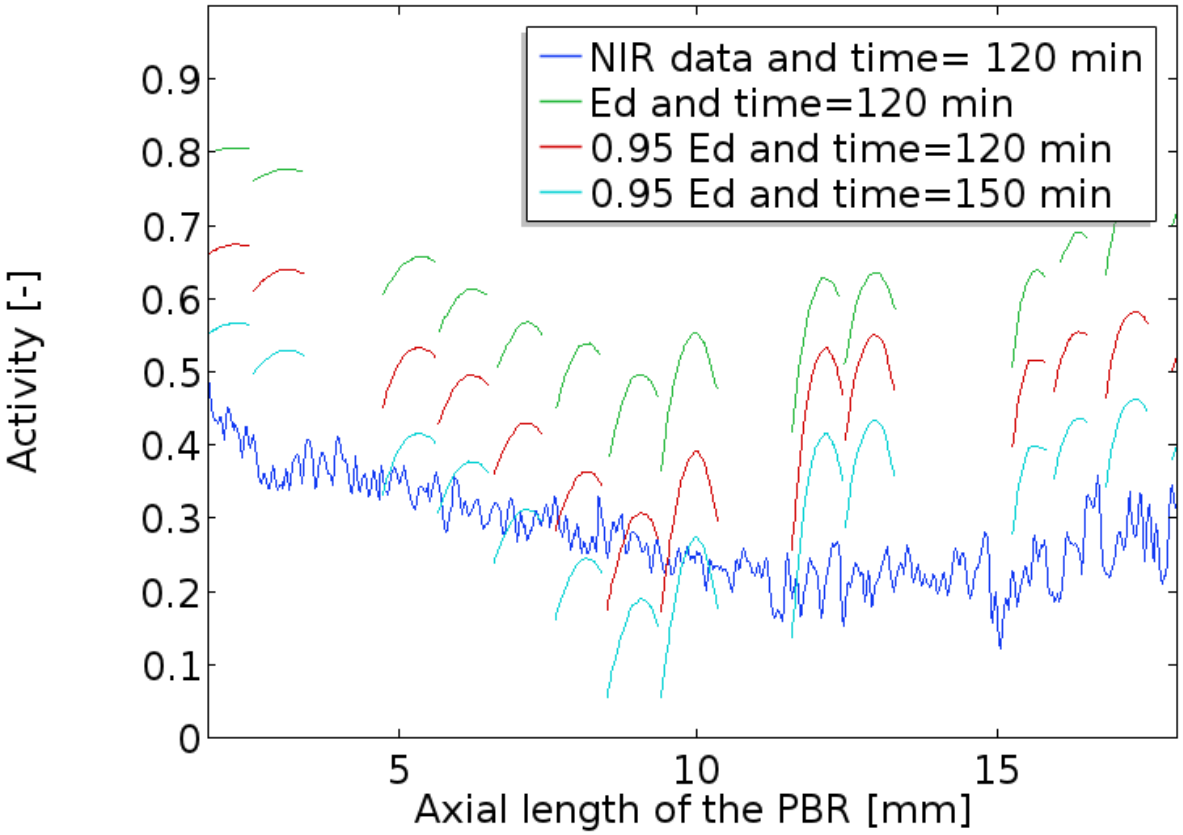

Figure 14 Profiles of circumferentially and radially averaged activity by NIR tomography (blue line) and simulation results of axial activity at two time-on-stream and two activation energy of deactivation, PBR of 10 mm ID, 25 mm length and AR of 10 — i.e., particle size of 1 mm, feed flow rate of 470 cm^3 min^{-1} and composition: 1.1 mol% at steady-state and increased to 1.4 mol% CO at transient conditions along with deactivation, 1.7 mol% H_2 and N_2 as carrier gas